2016

Measurements Of Electrostatic Double Layer Potentials With Atomic Force Microscopy

Jason Giamberardino
University of South Carolina

Measurements Of Electrostatic Double Layer Potentials With Atomic Force Microscopy

by

Jason Giamberardino

Bachelor of Science
University of South Carolina 2010

Submitted in Partial Fulfillment of the Requirements

for the Degree of Master of Science in

Physics

College of Arts and Sciences

University of South Carolina

2016

Accepted by:

Scott Crittenden, Director of Thesis

Bret Altschul, Reader

Cheryl L. Addy, Vice Provost and Dean of the Graduate School

Abstract

The aim of this thesis is to provide a thorough description of the development of theory and experiment pertaining to the electrostatic double layer (EDL) in aqueous electrolytic systems. The EDL is an important physical element of many systems and its behavior has been of interest to scientists for many decades. Because many areas of science and engineering move to test, build, and understand systems at smaller and smaller scales, this work focuses on nanoscopic experimental investigations of the EDL. In that vein, atomic force microscopy (AFM) will be introduced and discussed as a tool for making high spatial resolution measurements of the solid-liquid interface, culminating in a description of the development of a method for completely characterizing the EDL.

This thesis first explores, in a semi-historical fashion, the development of the various models and theories that are used to describe the electrostatic double layer. Later, various experimental techniques and ideas are addressed as ways to make measurements of interesting characteristics of the EDL. Finally, a newly developed approach to measuring the EDL system with AFM is introduced. This approach relies on both implementation of existing theoretical models with slight modifications as well as a unique experimental measurement scheme. The model proposed clarifies previous ambiguities in definitions of various parameters pertaining to measurements of the EDL and also can be used to fully characterize the system in a way not yet demonstrated.

Table of Contents

List of Figures

Chapter 1

Introduction

Whenever a solid object is placed into a solution containing ions, charge accumulation can occur at the solid-liquid interface. An initially charged object in any medium will attract opposite (counter) charges from any nearby sources. In the case of an electrode in solution, the source of the counter charges will come from any dissolved ions or from the solvent molecules themselves. The charges can be cations or anions from the electrolytic species present as well or, in the case of an aqueous solution, positively charged hydronium or negatively charged hydroxide molecules.

Even if the conductor is initially uncharged, a net charge will develop on its surface and the charge migration is thus initiated. A net charge can develop on such a neutral conductor via a variety of physiochemical processes. Two dominant sources of charging are surface group ionization or dissociation (i.e $\mathrm{COOH} \rightarrow \mathrm{COO}^- + H^+$) and entropic forces that result from the asymmetry created by the interface versus an infinite solution environment and drive ions toward the solid surface. No matter how the surface charge develops, what is important is the fact that the surface, now charged, will attract counter charges from solution and the region of space immediately surrounding the solid-liquid interface becomes filled with charges. This distribution of charges and counter charges at the interface are what form the EDL.

How the charges are distributed and what sort of electrostatic environment they create is a relevant question in many fields of science such as biology, biochemistry, soil sciences, mineralogy, chemistry, and solid state physics. This is because the presence of the EDL is what mediates all interactions that take place in liquid environments

of any kind. Whether it be colloids in a dispersion, cells in vivo, electrodes in a liquid cell battery, or any other system in which a solid-liquid interface is present, the EDL is present and plays a role in determining things like reaction rates, biological compatibility, or colloidal stability. Many models have been developed in the last 150 years to describe the electrostatic characteristics of the solid-liquid interface. Following the trend of much of modern science, the current goal of many researchers in the field is to probe the interface at smaller and smaller length scales.

The Crittenden Biophysics Laboratory is a lab with varied projects underway at any one time and possesses the equipment needed to make a wide array of physically relevant measurements. The core research of the lab, however, lies in utilizing AFM, which is a measurement technique that provides very high force resolution with high spatial resolution, as will be discussed in Chapter 3. Recently, my research interests have focused on using AFM to investigate the solid-liquid interface. Namely, I am currently attempting to characterize the EDL that forms at the interface in terms of the electrostatic potentials that develop within certain spatial regimes. In Chapter 2, I will discuss the development of the most widely accepted models of the EDL in chronological fashion. It is important to understand this developmental process as it gives a firm footing from which we can further develop new models and experimental techniques that rely on such models for the interpretation of experimental data.

The experimental techniques discussed will be centered around the use of AFM with some minor discussion of other techniques. For that reason, to supplement the discussion in Chapter 2, in Chapter 3, I delve into the full operational specifics of AFM, its capabilities, limitations, and its utility for nanoscale measurements of the EDL. Understanding how the instrument works and how it measures what it measures will provide a better foundation onto which the ideas of Chapter 2 can be built. Many other researchers have spent considerable time and resources asking similar questions to those asked in my work. Some have chosen to use AFM to answer their specific

questions as I have. So, in Chapter 4, I present a short literature review of some of the recent scientific developments in regards to measuring the characteristics of the EDL. This places my work in context and serves to introduce some terms and basic ideas for these types of measurements.

Finally, in Chapter 5, I will present the work I have completed in the area of nanoscale measurements of the EDL. This will include some theoretical and experimental research outcomes. The main result of the work presented within is a measurement of a particular potential drop that occurs on the solution side of the solid-liquid interface. This parameter has thus far only been measured once with AFM and my technique makes its measurement much simpler and more robust. A secondary outcome of the research presented is the ability to also measure the potential of the interior or bulk of a solution with respect to an external reference point.

Chapter 2

Models of the EDL

The development of models of the solid-liquid interface has been ongoing for over a century. Many scientists have contributed to the overall understanding of this system. A full treatment of all theories and their respective place within the larger knowledge structure is beyond the scope of this thesis. Here, instead, I will discuss a few of the major developments in the field relevant to my work in roughly chronological order.

Of course, there should be some metric by which the validity of each model can be tested. Early measurements of the solid-liquid interface were capable of measuring a quantity known as the differential capacitance and this served as the standard gauge of the veracity of a given model. It is, in fact, still a frequently reported parameter from experiments on solid-liquid interface systems. Typically measurements of the interface employ bias potential to an electrode that change quickly ($f \sim 1 - 1000\text{Hz}$) in time. The differential capacitance is a measure of how the system responds to such changing potentials. It is defined as $C_d = \frac{dQ}{dV}$, whereas the regular capacitance is defined as $C = \frac{Q}{\Delta V}$. The differential capacitance is then defined as the rate of charge accumulation divided by the rate of change of the potential difference. A further discussion of these ideas is saved for later chapters. It suffices for now that the differential capacitance will be used as the measure of a model's agreement with reality gleaned from experiment.

2.1 Helmholtz Model

Helmholtz is often credited as being the first scientist to investigate the solid-liquid interface and propose a model for this system. In a paper in 1853, often cited as that in which the first EDL theory was proposed, Helmholtz explored the electrical nature of the interface of two different conducting materials in contact or close to contacting one another[?]. He imagined a potential difference ΔV being applied to one of the conductors. Citing the fact that all excess charge on a conductor resides on its exterior surface, he proposed that imposing ΔV on a conductor would lead to surface charge density on this conductor. This charge would cause counter charges from the second, initially equilibrated, conductor to migrate toward its surface. He dubbed these two sheets of charge the "electric double layer".

In Helmholtz's simplified model, a monolayer sheet of charge forms at each surface. Helmholtz did not classify this system as a "capacitor", because the term was not introduced into the physical sciences vernacular until the 1920's[?]. Today, however, the system he described is recognized as just that. Helmholtz went on to derive an expression for the total charge, q, on the conductor surface as a function of the applied potential difference, ΔV, and the conductor separation distance, d. He found that

$$q = \frac{\epsilon\epsilon_0}{d}\Delta V. \tag{2.1}$$

Here, ϵ and ϵ_0 are the dielectric constant of the medium between the charge layers and the permittivity of free space, respectively.

If we choose to view the system as a capacitor, this leads to an expression for the capacitance, C of the system,

$$C = \frac{\epsilon\epsilon_0}{d}. \tag{2.2}$$

Therefore, the Helmholtz model predicts a capacitance that does not depend on potential difference or any factors other than the separation distance and the dielectric constant of the region between the two charge-carrying materials. Helmholtz cited

Gauss' result that the excess charge on a conductor will reside on its surface to derive his results and attempted to translate this result to the solid-liquid interface[**?**]. From the perspective of molecules on a solid conductor surface that has been immersed in a solution, however, the second conductor (the liquid) is essentially infinite in space and approaches infinitely close to the metal surface. This leads to an ambiguity of where the surface of the second conductor actually is located. Furthermore, the charges in a liquid are not bound to a particular lattice structure as they are in a metal conductor. These two discrepancies between a solid/solid and solid-liquid interface are why the predictions of the Helmholtz Model were not realized in experiment.

Measurements made by Grahame and others of the differential capacitance of NaF solutions in contact with a mercury droplet showed that it was not constant as proposed in the Helmholtz Model[**?**]. Grahame showed that the differential capacitance was a function of multiple factors including ionic concentration and applied voltage.

The underlying failure of this model to describe the solid-liquid interface, again, stems from the fact that Helmholtz was likely not considering that specific interface, but the more general case of two conducting materials close to contact. Due to the inability of this model to predict the easily measured differential capacitance, it became apparent that a new model was needed to quantitatively describe the charge distribution at the interface of a solid and liquid.

2.2 Gouy-Chapman Model

In the years between 1906 and 1915, Louis Georges Gouy and David Leonard Chapman independently considered the situation of a solid conductor immersed in an electrolytic solution[**?**, **?**] and sought to build on the work of Helmholtz. They both recognized that the major shortcoming of the Helmholtz model was its inability to describe the mobility of charges in the liquid phase. They both used thermodynamic techniques to solve the problem. Their approaches differed slightly, but they arrived

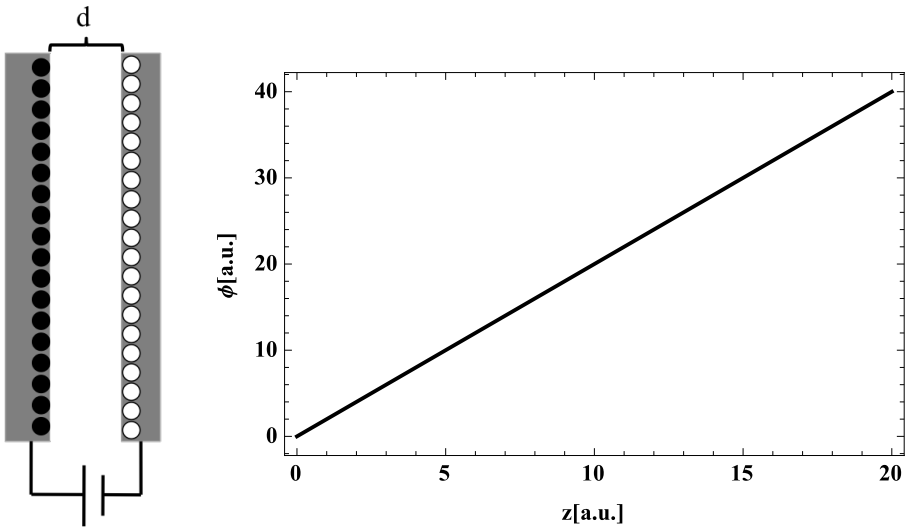

(a) (b)

Figure 2.1 The (a) charge and (b) potential distributions according to the Helmholtz theory. The two conductors develop equal and opposite surface charges, akin to a capacitor. Here, the charges are represented by black or white circles. The potential in this model is a linear function of the position the conductors, represented here by the value of z.

at the same result. Since they took slightly different approaches, I present an approach that is similar to both without being exactly equal to either. The process begins by writing the Poisson equation for a general charge distribution, which is

$$\nabla^2\phi = -\frac{\rho}{\epsilon\epsilon_0}. \tag{2.3}$$

Here, ∇^2 is the Laplacian differential operator, ϕ is the electric potential difference at some point with respect to infinity in Volts, ρ is the charge distribution measured in $\frac{C}{m^3}$, ϵ is the unitless dielectric constant of the solution and ϵ_0 is the permitivitty of free space in $\frac{F}{m}$. This equation relates the charge distribution in any region of space to the electrostatic potential that generates that charge distribution or vice versa. Gouy and Chapman realized that the thermal motion of the ions in solution would contribute a great deal to their overall energy profile.

Ludwig Boltzmann had recently derived a set of statistical relations with which one could calculate the probability for a number of particles to be in a particular

energy state. These relations hold true only if the temperature is high enough and/or the particle density is sufficiently low so as to neglect any quantum mechanical effects, which is generally the case for aqueous solutions at standard conditions. According to Boltzmann statistics, the concentration of any particular ionic species at any point in the solution is given by

$$C_i = C_{0i} \exp\left[-\frac{W_i}{kT}\right] \tag{2.4}$$

where C_{0i} is the initial or bulk concentration, W_i is the energy required to bring the ion in from infinity to the specified location, k is the Boltzmann Constant, and T is the temperature. The work required to move a certain charge depends on its valency, denoted by Z. This value reflects the excess charge on a particular molecule or atom and is also known as the "oxidation stat". For example, sodium has a Z of $+1$, whereas chlorine has a Z of -1. Therefore, the work term can be rewritten as

$$W_i = eZ_i\phi, \tag{2.5}$$

where e is the elementary charge, ϕ is the scalar electric potential, and Z_i is the valency of the ion species. Therefore, the local ion density will be

$$C_i = \sum_i C_{0i} \exp[-\frac{eZ_i\phi}{kT}], \tag{2.6}$$

and hence the local charge density, ρ will be

$$\rho = e\sum_i C_{0i}Z_i \exp\left[-\frac{eZ_i\phi}{kT}\right]. \tag{2.7}$$

Combining the (2.3) with this result yields

$$\nabla^2\phi = -\frac{e}{\epsilon\epsilon_0}\sum_i C_{0i}Z_i \exp[-\frac{eZ_i\phi}{kT}] \tag{2.8}$$

This is known as the Poisson-Boltzmann equation. It is a nonlinear second order differential equation. Equations of this type typically need to be solved numerically.

Solutions of (2.8) arise when one considers particular cases, such as different electrode (surface) geometries. Before considering any geometry, we note that we can

perform a Taylor series expansion of the exponential function itself, which includes a linear term followed by higher ordered terms. If the argument is considered to be small, the higher order terms become insignificant. In this case, the argument begins to get "small" when the electrostatic potential energy has a value much less than the thermal energy. That is, when $eZ_i\phi \ll kT$. For standard laboratory conditions, $kT \sim 4 \times 10^{-21}$J or ~25meV. In reality, the model agrees with experiment for values of the electrostatic potential up to ~75mV - 100mV[**?**]. Often, the procedure of expanding the exponential function and keeping only the linear term is known as the Debye-Hückel approximation or the Debye-Hückel Linearization. Doing so reduces (2.7) to

$$\sum_i C_{0i} \exp\left[-\frac{eZ_i\phi}{kT}\right] \approx \sum_i C_{0i} Z_i \left(1 - \frac{eZ_i\phi}{kT}\right). \tag{2.9}$$

Plugging this result back into (2.8) leads to

$$\nabla^2\phi = -\frac{e}{\epsilon\epsilon_0}\left(\sum_i C_{0i} Z_i - \sum_i \frac{C_{0i} e Z_i^2 \phi}{kT}\right). \tag{2.10}$$

The first term in this equation goes to zero due to the Nernst-Planck macroscopic electroneutrality principle of ionic solutions. This principle states that bulk ionic solutions tend to be electrically neutral with all cations having an anionic partner[**?**]. Using this, (2.10) reduces to

$$\nabla^2\phi = \frac{e^2\phi}{\epsilon\epsilon_0 kT} \sum_i C_{0i} Z_i^2. \tag{2.11}$$

This is known as the linearized Poisson-Boltzmann equation or the Linear Poisson-Boltzmann equation. This reflects the fact that the full Poisson-Boltzmann equation has been linearized by expanding the exponential and only keeping the term in the expansion that is linear in the potential, ϕ. This equation, unlike the full form of (2.8), can be solved analytically for different cases. The solutions of (2.11) vary depending on the particular geometry and boundary conditions being used. Here, we will go through two such examples that are relevant to the other work discussed in this thesis.

The 1-D Case

It is illustrative to consider the case of a planar surface with a potential distribution in solution that is only a function of a single spatial coordinate. Since (2.11) is a second order differential equation, it will require two boundary conditions to solve. In one dimension, one guesses a solution of the form

$$\phi(z) = C_1 \exp[-\kappa z] + C_2 \exp[\kappa z], \tag{2.12}$$

where $\kappa = \sqrt{\frac{e^2}{\epsilon\epsilon_0 kT} \sum_i C_{0i} Z_i^2}$. The boundary conditions are $\phi(z = 0) = \phi_0$ and $\phi(z = \infty) = 0$. The first condition is a definition of the "surface potential". This is the potential at the physical surface of the solid with respect to the bulk solution. The second boundary condition sets the potential at infinite distances from the surface to be zero. Plugging these into (2.12) yields $C_1 = \phi_0$ and $C_2 = 0$. Therefore,

$$\phi(z) = \phi_0 \exp[-\kappa z]. \tag{2.13}$$

This is the Gouy-Chapman result for the potential at any distance z from a planar surface due to the EDL that forms at the surface. The exponentially decaying charge distribution that results from this model is often referred to as the "diffuse layer" of a double layer system.

Note that the spatial potential distribution will be a function of several factors including the valency of the ionic species present, ionic concentration, ambient temperature, and the dielectric constant of the medium. Figures 2.3 through 2.5 demonstrate how these factors quantitatively affect the potential distribution. The figures also illustrate the general scales at which the various parts of these systems exist.

It is obvious how some of these parameters can be changed within the course of an experiment. For instance, the temperature can be adjusted by means of a heating element placed within the solution or simply increasing the ambient temperature. However, the dielectric constant of the solution is more complicated to understand.

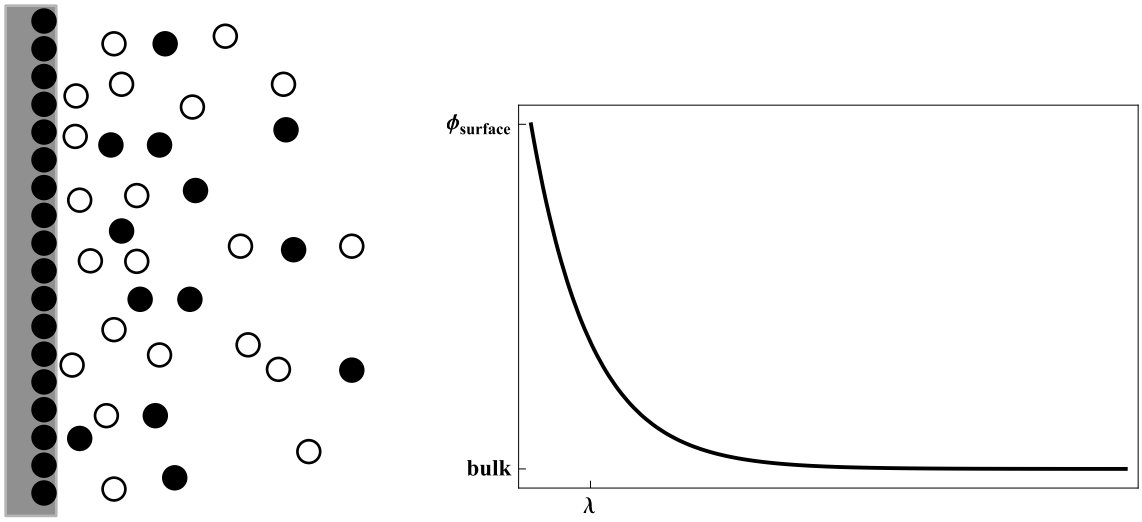

(a) (b)

Figure 2.2 The (a) charge and (b) potential distributions in the 1-D Gouy-Chapman model. Both the charge and potential drop exponentially from the surface value to the bulk value.

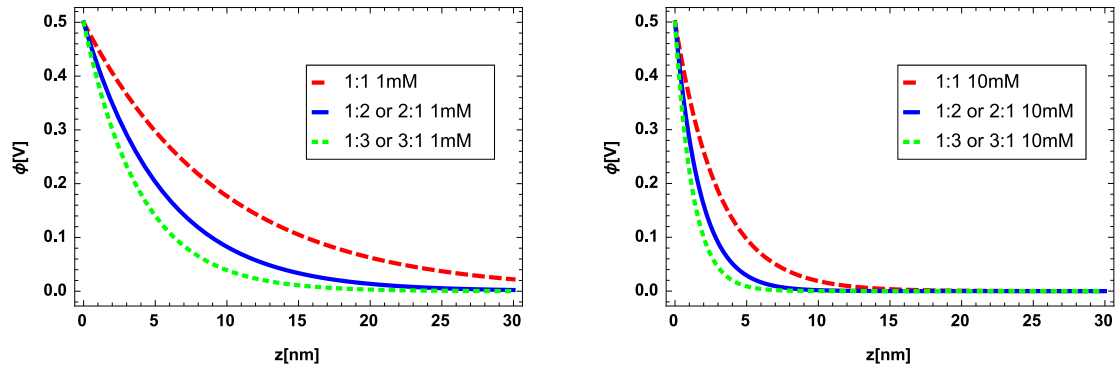

(a) (b)

Figure 2.3 Dependence of the spatial potential distribution on the valency of the salt present in solution. (a) Shows the potential profile of multiple valency salts present at 1mM concentration while (b) shows the profile for the same valency salts at a 10mM concentration.

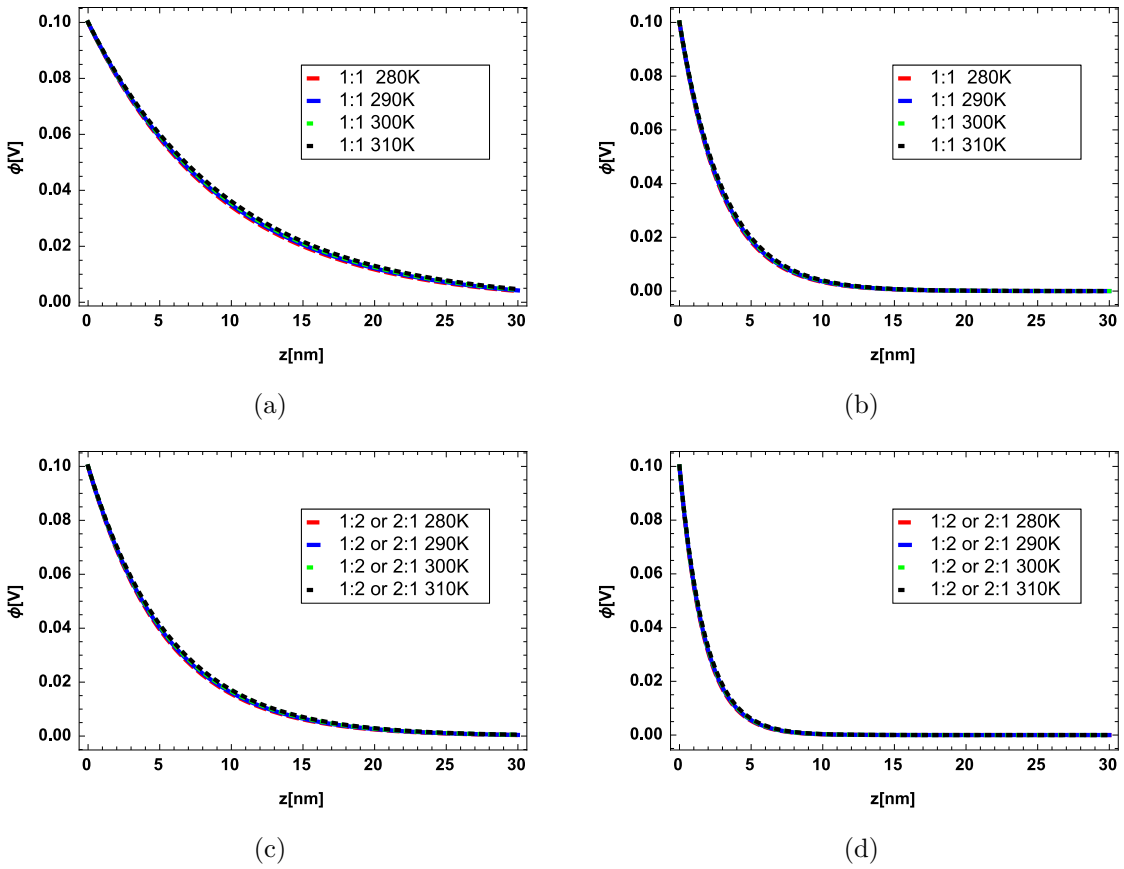

Figure 2.4 The temperature dependence of the potential distribution for (a) 1mM 1:1 salts, (b) 10mM 1:1 salts, (c) 1mM 1:2 salts and (d) 10mM 1:2 salts.

It's reasonable to assume that the addition of salts will affect its value, but to what extent? Experimental data and models have been combined in a number of studies to show that the addition of ions actually has little to no effect on the static dielectric constant of water for concentrations below $\sim$ 2M[**?**]. A number of reasons for the lack of effect have been proposed. For instance, Wang et al. suggest that water molecules, being very polar on their own, respond to the presence of an electric field much more strongly and thus will dominate the overall response of the solution to an external field, even in the presence of other ionic species[**?**]. Another possible explanation is simply that the number of present at concentrations under 1M is not enough to influence the response of an aqueous solution to an applied field, regardless of the polarizability of either type of molecule[**?**]. Whatever the reason, the bulk dielectric

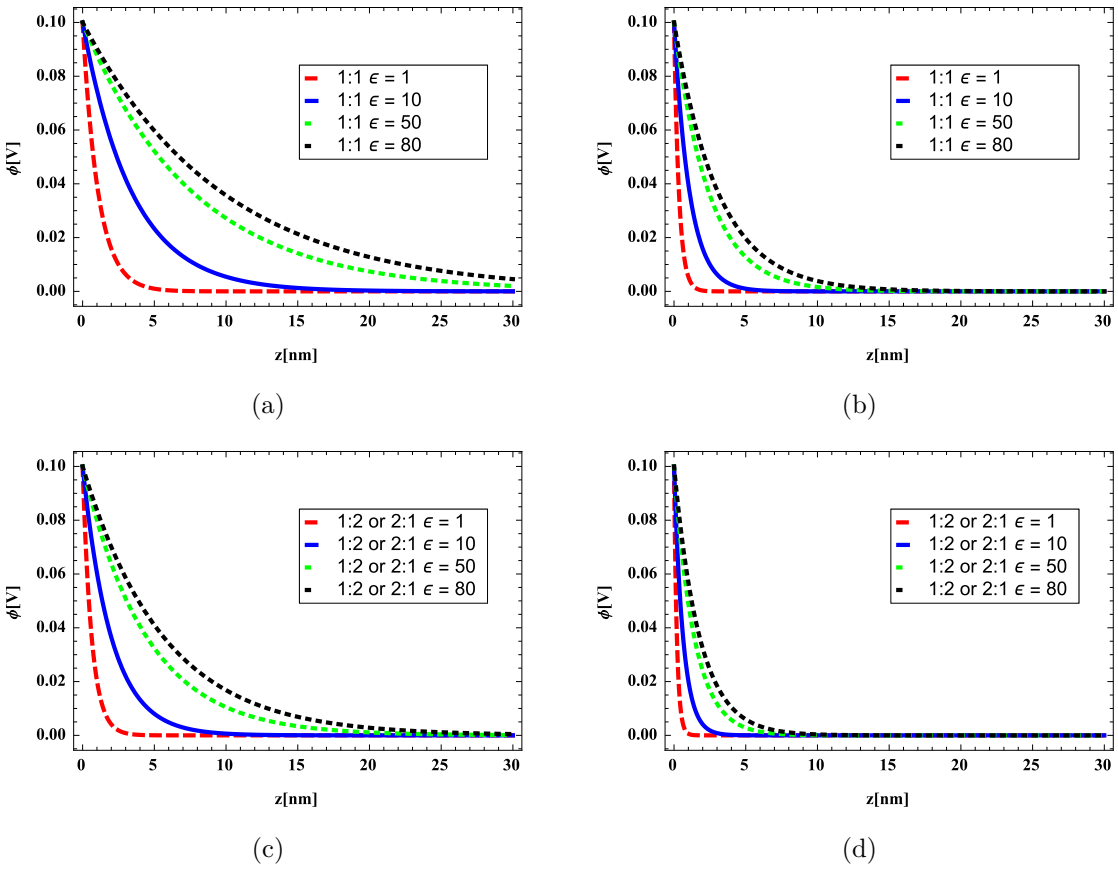

Figure 2.5 Dependence of the spatial potential distribution on the dielectric constant of the supporting medium. Each of the plots represents solutions of different valnency salts at different concentrations. (a) and (b) show the values for 1mM and 10mM 1:1 salts, respectively and (c) and (d) show values for a 1mM and 10mM 1:2 salt, respectively. The dielectric constant of water used in most applications of theory is ∼80.

constant of aqueous electrolytic solutions under 1M can be considered to be $\epsilon \sim 80$[**?**]. As will be discussed in Chapter 5, the dielectric constant of the medium at distances under 5nm from a surface can be much different than the bulk value. It is common, however, to assume it is constant throughout space.

Potential of a Spherical Particle

In general, the 3-dimensional case is the one of most interest because it gives the most accurate representation of a real world scenario. In 3D, the the simplest surface

one could imagine introducing into the theory is a spherical one. This geometry will be of particular importance in the context of future chapters. It provides a useful symmetry and allows for a convenient transition to spherical coordinates. In spherical coordinates,

$$\nabla^2(r,\theta,\psi) = \frac{1}{r^2}\frac{\partial}{\partial r}(r^2\frac{\partial}{\partial r}) + \frac{1}{r^2\sin\theta}\frac{\partial}{\partial\theta}(\sin\theta\frac{\partial}{\partial\theta}) + \frac{1}{r^2\sin\theta}\frac{\partial^2}{\partial\psi^2} \tag{2.14}$$

To reduce this complex expression, several approximations are made. First, the radius of curvature of the sphere is assumed to be much larger than the Debye length for the system is question. In the very large radius limit, the spherical surface essentially becomes a plane. In this case, only the radial component of the potential will survive. Assuming the potential has only a radial component and applying the chain rule to the first term of (2.14) yields

$$\frac{d^2\phi}{dr^2} + \frac{2}{r}\frac{d\phi}{dr} = -\frac{\rho}{\epsilon\epsilon_0}. \tag{2.15}$$

Using the form of the charge distribution given by (2.7),

$$\frac{d^2\phi}{dr^2} + \frac{2}{r}\frac{d\phi}{dr} = -\frac{e}{\epsilon\epsilon_0}\sum_i C_{0i}Z_i\exp\left[-\frac{eZ_i\phi}{kT}\right]. \tag{2.16}$$

Again, the exponential term is expanded assuming low potentials compared to the thermal energy. Similar to (2.11), this gives

$$\begin{aligned}\frac{d^2\phi}{dr^2} + \frac{2}{r}\frac{d\phi}{dr} &= \frac{e^2\phi}{\epsilon\epsilon_0 kT}\sum_i C_{0i}Z_i^2 \\ &= \kappa^2\phi,\end{aligned} \tag{2.17}$$

where, again,

$$\kappa = \sqrt{\frac{e^2}{\epsilon\epsilon_0 kT}\sum_i C_{0i}Z_i^2}. \tag{2.18}$$

This equation has the solution

$$\phi(r) = C_1\frac{\exp[-\kappa r]}{r} + C_2\frac{\exp[\kappa r]}{2r\kappa}. \tag{2.19}$$

To find the constants C_1 and C_2, two boundary conditions are once again needed. Similar boundary conditions as those used in the 1D case are used. They are $\phi(r = R) = \phi_0$ and $\phi(r = \infty) = 0$. Plugging these boundary conditions into (2.19) yields $C_1 = \phi_0$ and $C_2 = 0$. Again, ϕ_0 is the potential difference between the bulk solution and the physical surface and R is the radius of the surface in question. Combining all these results, the potential of a spherical particle placed in an electrolytic solution is given by

$$\phi(r) = \phi_0 \frac{R}{r} \exp[-\kappa(r - R)]. \tag{2.20}$$

The parameter κ that appears in both the 1D and 3D cases is often referred to the inverse screening length or the inverse Debye Length. That is $\kappa^{-1} = \lambda$ is the Debye Length. The potential at a distance of one Debye Length from the surface is a factor of e smaller than the potential at the surface. From (2.18), it is evident that the Debye Length is dependent on the bulk concentrations and valencies of the ions present in solution as well at the temperature and dielectric constant of the solution. Interestingly, the conditions on the surface, such as the potential, do not affect the screening length. It is a property purely of the solution.

2.3 Stern Model

As with the model proposed by Helmholtz, the Gouy-Chapman model failed to accurately predict the differential capacitance of solid-liquid interface systems. In fact, the differential capacitance predicted in the Gouy-Chapman model rises infinitely with increasing surface potential, ϕ_0. This result disagreed with the measurements of Grahame and others for surface potentials more than $\sim 100mV$ above the potential of zero charge (PZC), which is the externally applied potential at which no double layer is formed. At smaller applied potentials, however, the model and experiment agreed somewhat.

The infinite capacitance predicted by Gouy and Chapman arises from the fact that the continuum charge distributions used in their models failed to account for the finite size of ions and thus charges in the Gouy-Chapman model could approach infinitely close the the solid surface. To overcome this, Stern proposed a model that can be thought of as a combination of the Helmholtz model and the Gouy-Chapman model.

Stern proposed a modification to the Gouy-Chapman model asserting that that ions in solution could not approach infinitely close to the surface. He declared that the distance of closest approach of an ion was its hydrated radius. When this idea is introduced, it leads to a charge distribution that consists of a single layer of charges parallel to the solid surface, termed the "Stern Layer", with increasingly mobile and decreasingly densely packed charges further from the surface in the diffuse layer.

The potential produced by such a charge distribution is an initially linear potential drop across the Stern layer of charges, followed by an exponential potential drop though the diffuse layer. The potential on the solid surface with respect to the bulk solution is the "surface potential",ϕ_0. The potential at the outer boundary of the Stern Layer with respect to the bulk solution is known as the "Stern Potential", ϕ_{Stern}. Therefore the potential distribution, in this case for a planar object, in the Stern model is given by

$$\phi(z) = \begin{cases} \frac{\phi_{Stern}-\phi_0}{d_{Stern}} z + \phi_0 & z \leq d_{Stern} \\ \phi_0 + \phi_{Stern} \exp[-\kappa z] & z > d_{Stern}. \end{cases}$$

Here, d_{Stern} is the thickness of the stern layer, which extends from the surface and terminates at the centers of the solvated ions forming the Stern layer.

The Stern layer can be implemented into models with varying degrees of complexity. The layer can be considered to consist solely of solvated counterions, or be a mixture of solvated counterions and solvent molecules (partially filled circles in Figure 2.6(a)), or it could form from some specifically adsorbed ions, or some combination of

all of these. The specific adsorption of ions to the surface takes place when covalent bonds are formed between the ions in solution and the atomic of the solid surface. Furthermore, the strength of the ions' bond to the surface can have a large impact on the dielectric properties of the Stern layer. For these reasons and others, a great deal of the current work on the solid-liquid interface is focused on understanding the behavior of the Stern layer.

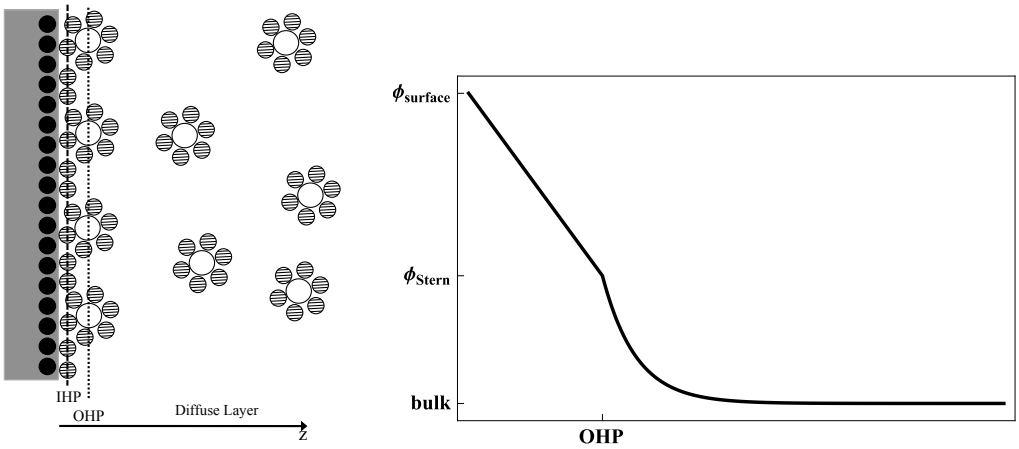

(a) (b)

Figure 2.6 The (a) charge and (b) potential distribution according the Stern model. The charge on the metal surface (filled circles) attracts counterions in solution(unfilled circles). The distance of closest approach of the counterions is defined by the Outer Helmholtz Plane (OHP). The potential drops linearly through the Stern layer out to the OHP and then exponentially through the diffuse layer to the bulk value. The Inner Helmholtz Plane (IHP) is not considered in this potential profile.

2.4 Grahame's Contribution

Grahame contributed to both the experimental and theoretical treatments of the solid-liquid interface. In 1947, he wrote a review of the Gouy-Chapman and Stern interpretations of the EDL. In it, he also expanded on the ideas of Stern. He proposed that the solvent molecules could potentially form the first, compact layer adjacent to the electrode surface. Along with solvent molecules, Grahame posited that even

uncharged molecules could specifically adsorb to the surface[?]. The next layer, he proposed, would be comprised of solvated ions. This led to the defining of two planes. The plane parallel to the surface at a distance of one solvent molecule radius is called the "Inner Helmholtz Plane" (IHP). Parallel to the IHP and located a distance of one solvated ionic radius from the surface is the "Outer Helmholtz plane" (OHP).The region beyond the OHP is the diffuse layer defined in the Gouy-Chapman Model. Figure 2.6(a) gives a schematic representation of the Inner and Outer Helmholtz Planes and their positions with respect to a surface. Beyond this, Grahame also derived an expression for the surface charge density present in the whole double layer as a function of the potential drop across the diffuse layer. He showed that

$$\sigma = \sqrt{8c_0\epsilon\epsilon_0 kT}\sinh\left(\frac{e\phi_0}{2kT}\right), \tag{2.21}$$

where ϕ_0 is the potential difference between a point in the bulk solution and a point that lies on the OHP[?]. This is known as the Grahame equation. It was derived assuming that the solvated ions had a distance of closest approach to the surface given by the position of the OHP. A more detailed analysis of this theory will be discussed in the final chapter when it is applied to analyze data from this lab.

2.5 Further Refinement of Models

The theories laid out thus far have been what are called "continuum" models because they treat the solution, conditions of convent molecules and ions as perfectly continuous bodies. Although Stern and Grahame considered the finite size of solvated ions and declared a distance of closest approach to the surface based on this value, the discretness of their models stopped there. Much of the recent research in the field has focused on treating the system in a more discrete manner. This involves correcting for ion-ion interactions, steric crowding, etc. and typically relies on computational modeling[?, ?, ?, ?]. Those models that attempt to treat the ions discretely, but

the solvent in a primitive, continuum manner are referred to as "primitive models". Impressively, the models of Gouy, Chapman, Stern, and Grahame are more than sufficient to explain a wide array of solid-liquid interface phenomena without the need for the addition of discreteness[**?**, **?**].

2.6 Forces Due to Double Layer Interactions - DLVO Theory

While the models mentioned thus far were concerned with describing the charge distribution around an object in solution, researchers quickly began wondering if these theories could explain any well-studied phenomena. The first application of these models was put forth in an attempt to explain coagulation of colloids in solution. Aggregation of aqueous dispersions had been well-studied experimentally up to the 1940's, yet no quantitative model existed to explain the particular behaviors of such dispersions. Roughly simultaneously, Derjaguin and Landau and Verwey and Overbeek derived analytical theories that could quantitatively describe particulate coagulation in solution[**?**, **?**]. The theories from the two groups were derived slightly differently but arrived at similar results. Hence, the theory is collectively known as DLVO theory. In essence the theory combines the long-range EDL forces, which were described by Gouy, Chapman and Stern, with the close-range van der Waals forces to fully describe the interaction between colloids in solution.

This method was successful in explaining phenomena that were known only empirically previous to its development. For instance, DLVO theory yields a quantitative dependency between the coagulation rate and salt concentration in solution. It was the first theory to do so. DLVO theory does, however, also have its shortcomings. For example, it cannot explain the formation of colloid crystals or the stability of some colloidal dispersions[**?**, **?**]. The analytical foundation of this theory, however, still serves as the basis upon which most models of double layer interactions are based as will be seen in later chapters. First, however, Atomic Force Microscopy will be

introduced as a general nanoscopic measurement technique and then its applicability to measurements of the solid-liquid interface will be discussed.

Chapter 3

Atomic Force Microscopy (AFM)

Atomic Force Microscopy is the go-to tool for the measurement of nanoscale interactions in a variety of environmental conditions. The AFM is useful for ascertaining an array of physical properties of a sample such as elasticity, roughness, electrostatic potential difference or magnetic field strength. An AFM by definition, however, measures forces and only forces. By carefully crafting the experimental setup, one can extract the aforementioned properties, but to do so, one must be able to relate the force measured by the apparatus to the property in question. The lateral and vertical resolutions of the instrument are dependent on the particular choice of equipment. Many different operational modes have been developed to serve a myriad of experimental needs. However, the basic operational principles hold true for almost all operation modes. This section will serve as an introduction to the construction and operation of an AFM. Note that many details of equipment and specific designs will be limited to the type of instrument used in this lab (Nanotec Dulcinea control unit and Nanotec Lanza/Cervantes AFM heads).

3.1 How AFM Works

The standard AFM consists of a cantilever, laser, photodetector, a digital control unit, and at least two piezoactuators as depicted in Figure 3.1. There is, as will be shown, much more included in a real experimental setup. The microscopic cantilever is brought close to the surface via a 3D piezoelectric raster scanner mounted under the sample stage. The forces on the cantilever cause it to bend and this movement

is monitored via a reflected laser beam which is collected by the segmented photodetector.

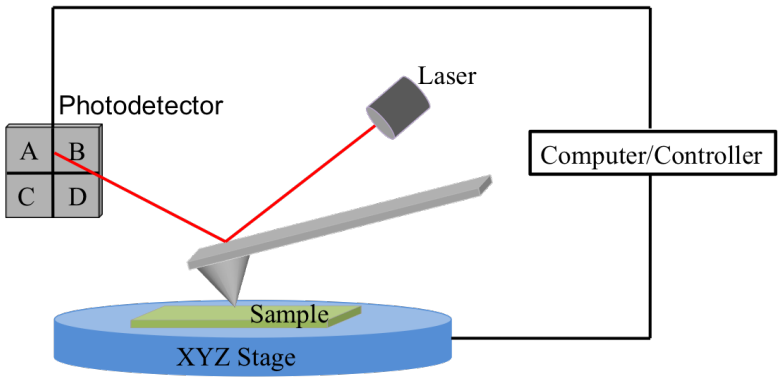

Figure 3.1 Schematic of a typical AFM system. The cantilever/tip system is brought near a sample and its three-dimensional movement is monitored via a laser beam that is reflected off the back surface of the cantilever. The reflected beam is collected at a quad-segment photodetector and a computer controlled feedback system is used to adjust the position of the sample according to various feedback input parameters defend by the user.

The cantilever is usually $\sim 200\mu$m in length, $\sim 50\mu$m wide, and $\sim 1\mu$m thick. The cantilever generally contains a sharpened conical tip which is defined by its height, nominal radius, and cone angle. The cantilever and tip's geometrical dimensions have a large impact on the force sensitivity of the AFM system. Typical commercially available cantilever tips are $\sim 20\mu$m long, with a half cone angle of $\sim 30°$, and a nominal radius of $\sim$50nm. Systems employing these cantilevers have typical lateral resolution of $\sim$30nm and vertical resolution of $\sim$5 Å. Cantilevers are etched from silicon or a silicon-based composite material and can be treated with a variety of coatings to alter their behavior under different experimental conditions. For example, gold and platinum coatings are frequently used to make the cantilever a conductor of electrical current. In terms of modeling, the cantilever/tip system is almost always considered to be comprised of a beam, truncated cone, and sphere embedded at the end of the cone.

The laser uses light generally in the visible range with wavelengths $\sim$500nm and

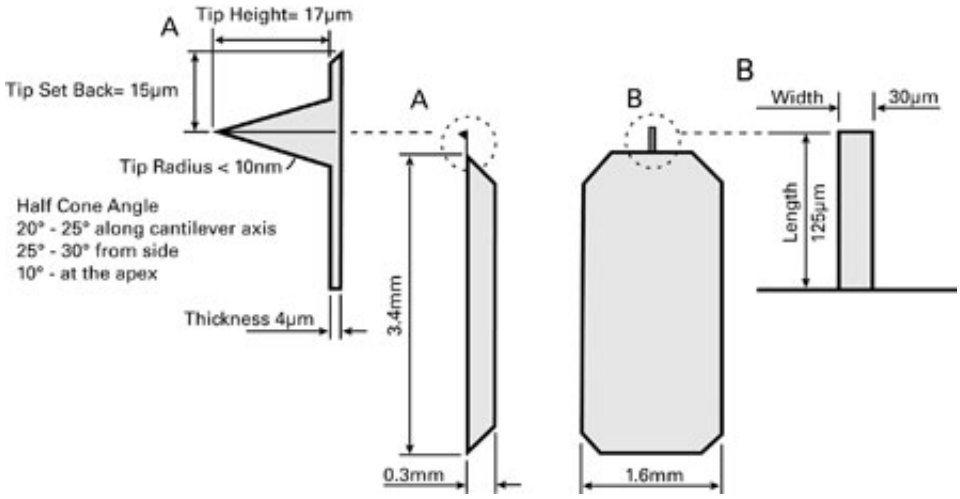

Figure 3.2 Schematic of a typical AFM cantilever on a larger silicon chip. Image courtesy of Budget Sensors ®.

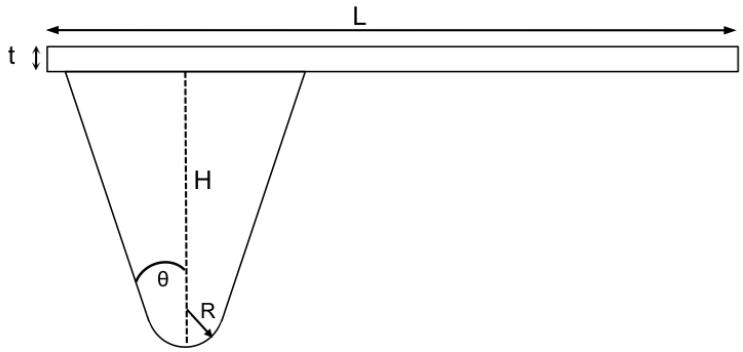

Figure 3.3 The standard model for the AFM cantilever/tip system. The cantilever is a flat beam of length L, width w (not represented), and thickness t. The tip is composed of a truncated cone, with characteristic height, H, and angle θ with a sphere of radius R embedded at the end.

power ∼5mW. It is shone onto the back of the cantilever and the reflected beam is used as a proxy to measure the movement of the cantilever. The motion of the reflected beam is measured by a quad-segment photodetector as shown in Figure 3.1. The photodetector measures the position of the reflected beam in a 2-D plane, which can be related to the 3-D motion of the cantilever. Each position of the laser spot on the silicon detector generates a current which is converted to a voltage and then sent to the digital controller unit. Segments labeled A, B, C, and D have

respective voltages of V_A, V_B, V_C, and V_D. The current generated is dependent on what fraction of the beam is radiated on each of the four segments of the detector. For this reason, the beam diameter is an important parameter and generally needs to be on the order of the side length of one of the four square segments. In order to actually convert the beam position to cantilever motion, the detector registers the amount of light entering each segment. This information is passed to the computer, which runs through a simple calculation. To monitor the vertical displacement of the cantilever, the computer calculates $(V_A + V_B) - (V_C + V_D)$. To monitor the horizontal displacement, the computer calculates $(V_A + V_C) - (V_B + V_D)$. With knowledge of the displacement in each direction and the effective spring constant of the cantilever, one can calculate the force on the cantilever in each direction. One of the piezoactuators, the piezo scanner, is used to move the sample or cantilever/tip system in the x-y plane in order to scan and acquire data over a specified area. The range of standard piezo scanners is $\sim 10\mu$m.

3.2 Operational Modes Of AFM

All operational modes of AFM require the use of a feedback system. In a feedback system, a signal which is an output of the measurement system is fed back into the system and used as an input measurement for some sort of modification or adjustment signal[**?**]. Specifically, AFM systems generally apply what is known as a Proportional-Integral-Derivative (PID) feedback mechanism. In this type of feedback system, the error or difference between an input signal and a desired value for that signal is minimized. To do so, the input signal is measured and an error is calculated between its value and the set point value. Then the system adjusts a particular control variable in order to further minimize the error. This cycle repeats until stopped by the user.

Each unit in the PID network functions slightly differently. The P unit uses a gain that is proportional (P) to the error signal as its input to the control variable.

The I unit uses a gain that is proportion to the integral (I) of the error signal as integrated over a certain number of previous cycles. The D unit uses a gain that is proportional to the derivative (D) of the error signal as a function of time as its input to the control variable process. The input value to the feedback can be a wide array of physical parameters and vary as the experiment demands. For the majority of AFM measurements, the control variable is the vertical position of the sample with respect to the AFM tip and the input signal is some property of the cantilever motion.

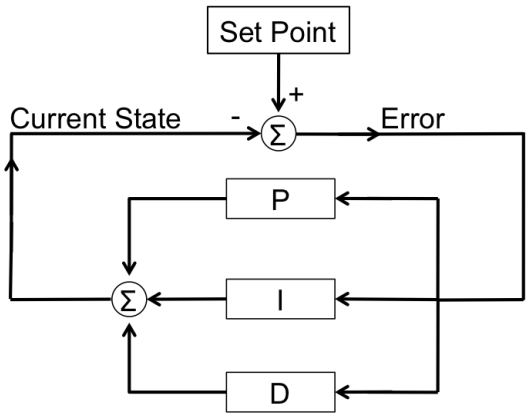

Figure 3.4 Block diagram of a PID feedback loop. A desired state is input by the user. The difference between that set point and the current state of the system (error) is calculated and used as the input for the PID network. The output is a control sequence which gives the system some instruction as to how to change its state. The process is then repeated continuously.

Contact Mode

In the simplest operational mode of AFM, the tip is brought into contact with the surface and scanned over a user-defined area. This is known as contact mode. The feedback parameter here is the z-compenent of the total force as measured by the photodetector. This is known as the "normal force". The feedback is usually employed to keep the normal force constant. In order to do so, the feedback output uses the piezo to move the sample in the z-direction, thus adjusting the deflection of the cantilever as it encounters objects or features on the surface. The voltage sent to

the piezo which is required to keep the normal force constant is then digitized and turned into a topographical representation of the surface. The piezo can be used to withdraw the sample far enough such that the tip and sample break contact.

Typically, one is interested in how the force on the cantilever varies with separation distance. So, a commonly employed measurement is a mapping of the force on the cantilever versus the z-position of the piezo. This is known as a “force-distance curve" or “F-Z curve” or “force curve”. A typical contact mode or “static” force curve taken in air or vacuum conditions is depicted in Figure 3.5.

In the figure, the blue dotted line represents the approach of the probe towards the sample and the red curve depicts the separation of the probe and sample. Force curves have a very distinctive structure that has been well explained and modeled in literature[**?**]. When the tip is far from the surface (A in Figure 3.5), there is no force and the cantilever deflection (force) is zero. Once the tip is brought close enough ($\sim$20nm) to the surface, long-range electrostatic forces tend to pull the cantilever towards the surface. As the tip gets close and van der Waals forces begin to have an impact, the total force gradient becomes larger than the elastic constant of the cantilever and there is an almost instantaneous jump to contact with the surface (B in Figure 3.5). This is known as “snap-in” or “snap-to-contact” or “jump-to-contact”. Now the tip and surface are in contact and move in unison with one another (B-D in Figure 3.5). As the sample is withdrawn from the tip, the adhesive forces between the two keep the tip “glued” to the surface until the elastic resting force of the cantilever is large enough to pull the sample and tip apart (E in Figure 3.5).This is sometimes referred to the “pull off”. One can see from the figure that the approach and withdrawal processes do not overlap when plotted with one another. One reason for this is a form of hysteresis in the system. This usually derives from the slight instability of the piezo scanner to return to exactly the same position vertical at which it started the measurement. Piezos are known to be hysteretic in this way.

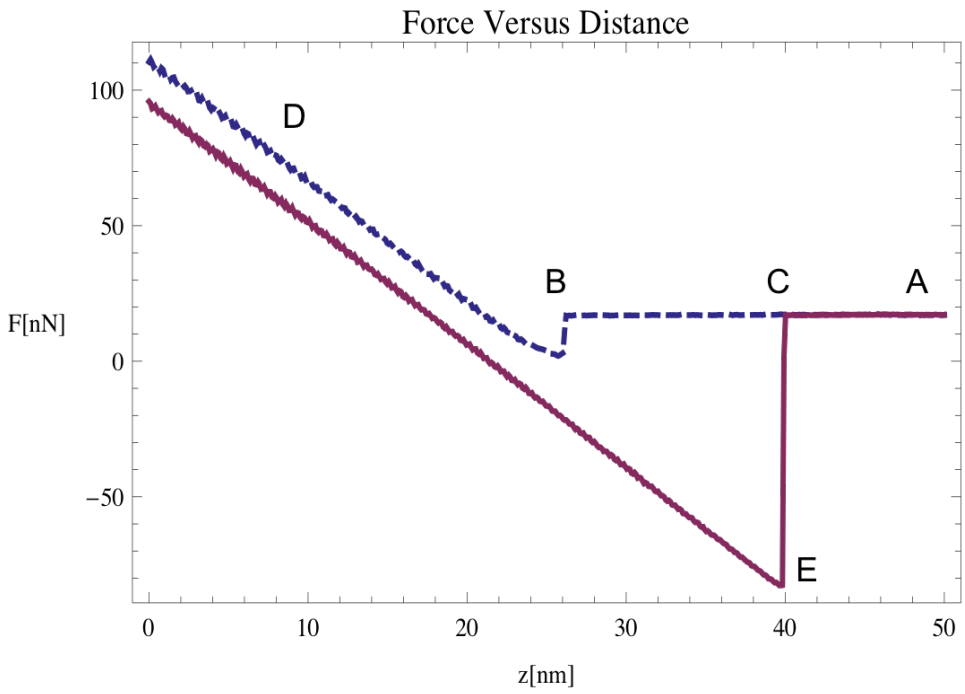

Figure 3.5 A representative force-distance curve measured in ambient laboratory conditions. The dashed line is the approach curve and the full line is the withdrawal curve. The cantilever begins far from the surface at zero deflection(A). As it approaches and the force gradient becomes larger than the spring constant, instantaneous jump to contact occurs(B). The sample and cantilever/tip are in contact and move in unison (B-D). The tip is withdrawn from the surface and eventually the adhesive forces are overcome and the tip and sample separate (E).

Furthermore, the adhesive forces between the tip and sample are much larger than the attractive van der Waals forces. This is the reason for the larger force required for pull off.

This mode can be destructive to highly compliant substrates and for that reason is rarely used for biological and other physically sensitive applications.

Non-Contact / Tapping Mode

A more nondestructive operational mode is one known as non-contact or tapping mode. In this mode, the cantilever is physically oscillated, usually at its resonance frequency, via a piezoelectric plate on which it rests, and scanned at a certain dis-

tance above the sample. The cantilever is typically kept far enough from the surface so that the attractive van der Waals forces do not cause a snap-to-contact. Due to the physical characteristics of the cantilever, it will oscillate at a particular amplitude and frequency. Forces such as van der Waals, long-range electrostatic, and air damping between the tip and surface result in a shift in the dynamic motion of the cantilever. Assuming the cantilever behaves like a simple harmonic oscillator, the cantilever will then undergo damped harmonic motion. The variations in the forces due to the interaction with the surface will cause changes in the oscillation amplitude and/or resonance frequency. The cantilever oscillations are monitored via a lock-in amplifier (LIA). Feedback is employed to keep one or more of the oscillation amplitude, oscillation frequency shift, or phase difference between the driving waveform and the cantilever oscillations constant. Once again, the feedback output is typically the z-position of the sample. Using feedback on any one or combination of the different parameters listed results in a different operational mode. For example, applying feedback to keep the oscillation amplitude or frequency constant is known as Amplitude Modulation AFM (AM-AFM) and Frequency Modulation AFM (FM-AFM), respectively. These modes and others like them are useful for gaining a quantitative measurement of the surface topography, adhesion, compliance, etc. One may be interested, however, in the electrical or magnetic properties of the sample. In the case of the electrical measurements, there exists a subset of operational modes, often collectively referred to as Electrostatic Force Microscopy (EFM).

KFM

By far, the most versatile and often used EFM mode is known as Kelvin Force Microscopy (KFM) or Kelvin Probe Microscopy (KPM). In this mode, an alternating AC potential is applied between the tip and substrate. This alters the harmonic motion of the cantilever by adding a new force to the tip/substrate interactions.

When a potential is applied between any two conductors, the resulting force has the form

$$F = \frac{1}{2}\frac{dC}{dz}V^2 \tag{3.1}$$

where C is the capacitance of the system, z is the direction whose unit vector points from one surface to the other, and V is the applied potential. In the case of KFM, $V = (V_{DC} - V_{CPD}) + V_{AC}\sin(\omega t)$, where V_{DC} is an applied static potential, V_{CPD} is the contact potential difference between the tip and sample, V_{AC} is the amplitude of the applied sinusoidal voltage, and ω is the frequency of oscillation of the AC potential. The contact potential difference arises from a difference in work functions between the electrons in two different metals. Due to the different work functions, which can be a factor of lattice structure, doping, or contamination, the electrons in the highest occupied state within one metal will be of a different energy than those in a different metal. Thus, there is an energy difference between them and this is the source of the Contact Potential Difference. Equation (3.1) now becomes

$$\begin{aligned} F &= \frac{1}{2}\frac{dC}{dz}[V_{DC} - V_{CPD} + V_{AC}\sin(\omega t)]^2 \\ &= \frac{1}{2}\frac{dC}{dz}(V_{DC} - V_{CPD})^2 + \frac{1}{4}\frac{dC}{dz}V_{AC}^2 + \frac{dC}{dz}(V_{DC} - V_{CPD})V_{AC}\sin(\omega t) \\ &- \frac{1}{4}\frac{dC}{dz}V_{AC}^2\cos(2\omega t), \end{aligned} \tag{3.2}$$

where the relation $\sin(x)^2 = \frac{1-\cos(2x)}{2}$ has been used.

It is evident from the above equations that the force between the tip due to the applied potential will be oscillatory in nature. Furthermore, it will have a static component and components that oscillate at ω and 2ω. That is

$$F = F_{static} + F_{\omega} + F_{2\omega}. \tag{3.3}$$

It is this fact that makes KFM a functional measurement technique. By setting ω properly, the cantilever can be oscillated at a desired frequency using the electrostatic interactions between it and the surface. A lock-in amplifier is employed to detect the

oscillation signal, which will have components due to the electrostatic interactions and the mechanical vibration. The LIA measures the input signal, performs a version of Fourier analysis and reports the amplitude of oscillation at a particular frequency. Many different measurements can be made once the cantilever is set in motion. For example, the contact potential difference between the surface and tip can be found by oscillating the cantilever using the AC potential while simultaneously applying a DC potential and varying its value. As seen above, the ω component of the force is dependent on $V_{DC} - V_{CPD}$. Thus, the force is minimized when the applied DC potential is equal to the contact potential difference. The characteristic plot of amplitude of oscillation versus applied DC voltage will have a minimum where $V_{DC} = V_{CPD}$ as seen in Figure 3.6. This is the most fundamental use of KFM. Of course, the

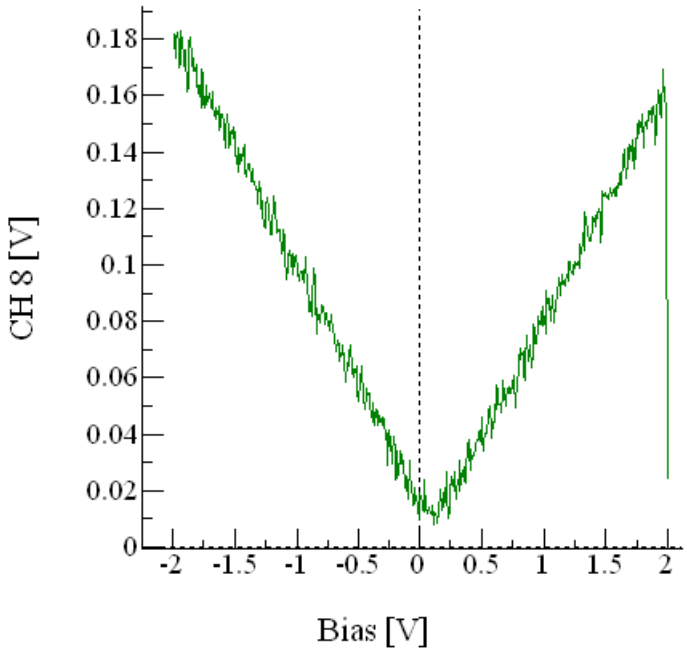

Figure 3.6 A characteristic "V Curve" showing the minimum in the oscillation amplitude, shown here as CH8, at ω due to the applied potential. The minimum occurs at an applied DC potential equal to the contact potential difference between the tip and the surface.

practical uses for this technique have been extended to measure new surface properties. Currently, a great deal of interest is being placed on performing these types of electrostatic measurements in liquid environments, as will be discussed in the next chapter.

Colloidal Force Microscopy

A versatile AFM technique for analyzing the solid-liquid interface is colloidal probe method or colloidal force microscopy. A colloid is roughly defined as a microscopic or larger molecule or particle that is dispersed in another substance. Colloidal Force Microscopy is a method used to understand the forces on such particles as they interact with other objects. In fact, the first measurement with AFM of the solid-liquid interface used this technique[**?**]. This technique involves performing static force measurements, making it simple, fast, and versatile. In general, a cantilever fitted with a colloidal probe is approached to a surface and the force is measured as a function of separation distance similar to the force measurements discussed in Chapter 2. The probe is often a microscopic sphere. The forces that cause static deflection are directly related to the electrostatic properties of the surface and probe and are unique to systems in ion-containing liquid media. The spherical geometry of the probe makes analysis of these forces easier since most basic force models used to describe forces on colloids such as those in DLVO theory assume a spherical particle shape.

The relatively large radial dimensions of the typical colloidal probe also increase the signal to noise ratio while also minimizing the contributions from other components of the system such as the cantilever itself. The large probe size presents a downside as well. The lateral resolution of this method is very poor compared to techniques that employ sharp, nanoscopic tips.

Now that the basic operational principles and modes of AFM are understood, we

can turn our attention to the specific systems of interest to the research presented in this thesis. Namely, we will discuss the various experimental approaches used to understand the electrostatic properties of the solid-liquid interface.

Chapter 4

Measurements of the EDL

Recently, there has been a great deal of interest in the exploration and measurement of the solid-liquid interface. Simultaneously, many have become interested in understanding nanoscopic electrical interactions in liquid environments. Various paths have been taken to describe and probe this interface and, more importantly to this work, to understand electrical behavior at small scales in liquids. This section serves as a brief literature review of some representative theoretical and experimental developments that have been made that are relevant to the original work found in Chapter 5 of this document.

4.1 Electrostatic Actuation in Conducting Liquids

Panchawagh et al., in 2009, developed a model and performed experiments measuring the dynamics of microscopic actuators operated in conducting media[**?**]. They were concerned with the frequency dependence of the displacement of comb-drive and parallel plate actuators, which are two commonly used microelectromechanical devices (MEMs). In both systems, a potential was applied between a mobile electrode, which was suspended via a spring, and a fixed electrode. Opposite charges gather on the electrodes and an attractive force develops between them. The applied potential was varied within a certain range of frequencies.

To analyze the system, they developed a model which viewed the system as a simple RC electrical circuit and all parameters of interest were calculated or derived from there. Two electrodes were considered to be plates of a capacitor. Each plate was

coated with a passivation layer characterized by its permittivity and resistance. The passivation layer was put in place for purposes important for practical engineering and adds little to no complication to the physical system. The conducting liquid media between the two plates was characterized by its conductivity and capacitance. Using this simple analysis, they were able to model the dynamical behavior of both the parallel plate and comb-like actuator systems. They showed that the position and stability of the mobile plates were dependent on the frequency and amplitude of the applied AC potential.

Moreover, they calculated the force on the electrodes as a function of frequency and voltage and found the critical frequency at which the actuation force due to the applied potential overcomes the restoring force of the spring and the plates "pull in" to contact. After calculating this critical frequency and using it as a known parameter, the experimental data did not fit the model prediction for displacement as a function of frequency as shown in Figure 4.1. While the form of the dependence (sigmoidal) is predicted correctly, the experimental data was shifted versus the model prediction. The authors gave a list of possible causes for a shift in the entire data set. They included the possible difference in liquid conductivity for small volumes versus bulk liquid, unknown native oxide layer thickness and hence dielectric response, and dissolution of salts or evaporation of the conducting liquid which would affect its electrical response.

4.2 EFM/KFM in Liquids

Gramse et al. performed a number of experiments focused on electrical measurements in liquid media with AFM for several years. They first developed a method with which it is possible to measure the local dielectric properties of surfaces in conducting liquid media[?]. They then applied this technique to measure the dielectric constant of biological components bound to a surface[?]. In order to do so, they modeled the

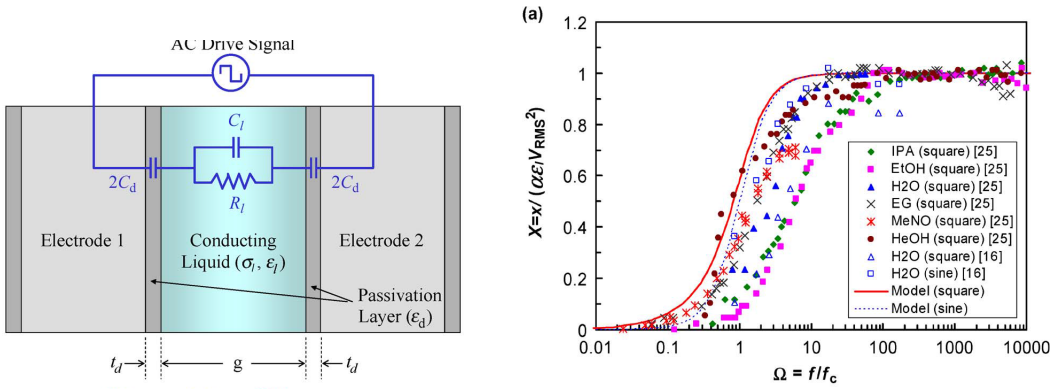

Figure 4.1 (a) Schematic representing the equivalent circuit analysis as employed by Panchawagh et al. Two electrodes are immersed in a conducting fluid and an AC potential is applied. Each electrode is coated in a dielectric passivation layer with permittivity ϵ_d and capacitance C_d. The fluid between the plates is characterized by its conductivity σ_l, dielectric constant ϵ_l, resistance R_l, and capacitance C_l. (b) Amplitude of cantilever oscillation versus normalized applied bias frequency for a number of different fluids (labeled in the inset of the plot). ®[2009] IEEE

system using an equivalent circuit analysis. They considered the cantilever and tip as separate and found the critical actuation frequencies for each. The frequency here is that with which the potential between the tip and sample is oscillated.

They found that the critical frequency for the cantilever is in the 10 kHz range, whereas for the tip, it is in the 10 MHz range. This implies that the cantilever will contribute more to the interaction force than the tip at low frequencies and vice versa. One expects that if the tip is the major contributor to the force, the force resolution will be higher for higher frequencies. To test this, they performed dielectric spectroscopic measurements over a patterned surface in aqueous electrolytic solutions at varying frequencies. The sample was a surface with intermittent stripes of Si^{2+} and SiO_2.

It was shown that at high frequencies, the resolution increases and the pattern becomes more distinguished as in Figure 4.2(b). This implies that the system is becoming increasingly sensitive to changes in the electrical properties of the surface.

Next, they used force-distance curves to quantify the capacitance and dielectric

constants of the Si^{2+} and SiO_2 surfaces, respectively. The data is shown in Figure 4.2(c). Again, they did so while applying bias potentials at frequencies ranging from 10KHz to 20 MHz and showed that the sensitivity of these measurements increases as the applied frequency increases. Their results of 1.1 $\mu F/cm^2$ and 4.4 $\pm$ 0.5 for the capacitance and dielectric constant of Si^{2+} and SiO_2, respectively, agree well with values found in literature.

So for this technique to be used, one must apply frequencies in the range of 10 MHz. The purpose for such high applied bias frequencies is that variations in the potential will be fast enough to prevent the EDL from responding. Although the double layer was always present in these measurements, its contribution to the measured force was a constant offset since its structure remained constant. In essence, this method was developed as a way to remove the contributions from the mobile ions in the liquid phase. The authors wanted to develop a technique that made the solution between the probe and sample invisible in terms of forces. Hence, it will not serve as a good probe of the EDL.

Umeda et al. developed a method that allowed for frequency modulation AFM (FM-AFM) to be performed in liquid environments[**?**]. This method involved applying a bias potential between a cantilever which had a conductive coating on its back side and a thin conducting layer (indium tin oxide) deposited on a glass window above the cantilever. The coating allowed the laser light to pass through while simultaneously acting as a counter electrode for the cantilever. By varying the frequency of the applied bias between the cantilever and the coated electrode, they were able to oscillate the cantilever over a range of frequencies.

The advantage of this setup is that the potential is applied between the cantilever and a counter electrode that is not the sample. This means that the electrical properties of the sample do not affect the operation. Therefore, this method is uniquely capable of electrically exciting the cantilever with a non-conducting sample. The

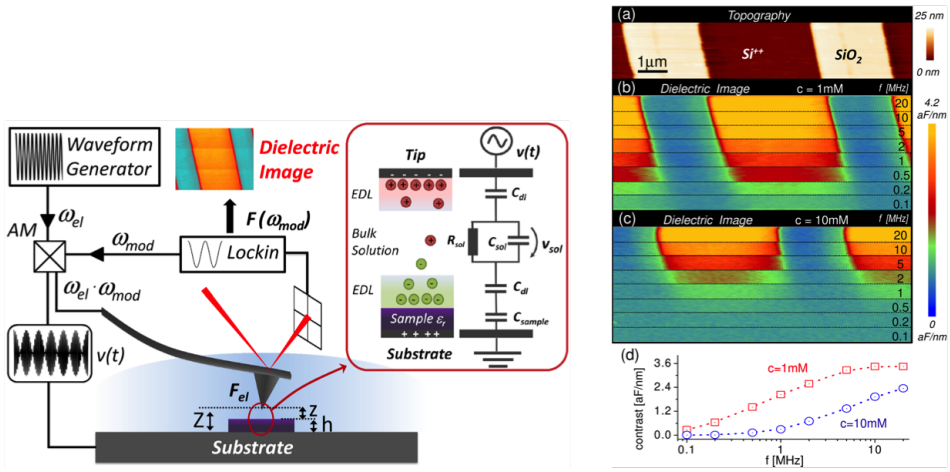

(a) (b)

(c)

Figure 4.2 (a) Schematic of the experimental setup for the work done by Gramse et al. (b) Topography and dielectric images for varying applied bias potential frequencies. It can be see that the resolution increases with increased frequency. That is the dielectric images map better and better to the topography image as the applied frequency increases. (c) Capacitive gradient vs. distance curves again for varying applied frequencies. Once again, it can be seen that increasing the applied bias potential frequency leads to higher capacitive gradients and hence interaction forces between the tip and sample. *Reprinted from Dynamic electrostatic force microscopy in liquid media, Gramse, G. and Edwards, M. A. and Fumagalli, L. and Gomila, G., Applied Physics Letters, 101, 213108 (2012), with the permission of AIP Publishing.

AFM was operated in frequency modulation mode when imaging was performed.

They found that at lower bias frequencies, the amplitude of oscillation is increased. Figure 4.3(b) shows the response of the system to such changes in applied bias frequency. This peculiarly large oscillation amplitude at low frequencies is attributed to surface stress forces. The surface stress force arises when charges from solution accumulate in an asymmetric fashion on the tip side and backside of the cantilever. The fact that the surface stress dominated the cantilever deflection at low frequencies is due to the formation of the EDL. At lower frequencies, the charges have more time to move toward their equilibrium positions around the cantilever.

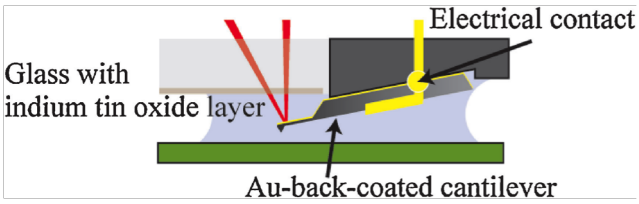

(a)

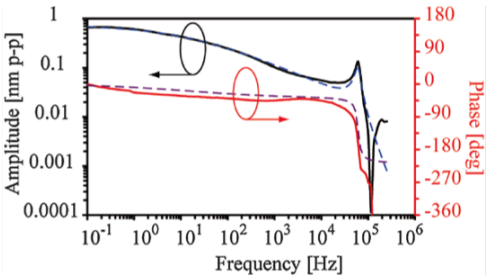

(b)

Figure 4.3 (a)Schematic of experimental setup for the first Umeda et al. paper in which FM-AFM in liquid with electrical cantilever stimulation was demonstrated. (b) Frequency response curves of the amplitude and phase of the cantilever. Dashed lines represent theoretical calculations and the solid lines represent experimental data. *Copyright 2010 The Japan Society of Applied Physics

After developing the unique method for electrostatic actuation in fluids with non-conducting samples, the same group further evaluated the capacitive forces acting on a cantilever at the solid-liquid interface[?]. They concluded that the overall deflection of the cantilever has contributions from the electrostatic force as well as the surface stress forces as stated in their previous work. In this work, they also evaluated the

effect of the solvent polarity on the forces acting between the tip and sample. To test this effect, measurements of the force versus frequency and force versus tip-sample distance were done in a number of different solvents. The solvents were grouped into three categories: non-polar, protic polar, and aprotic polar. The non-polar solvent was fluorocarbon liquid. Aqueous potassium chloride (KCl) and acetic acid were used as the protic polar solvents. The aprotic polar solvent was acetonitrile.

At first, the frequency response far from the surface was tested in all solvents. The amplitude versus applied AC frequency showed the anomalous behavior at low frequencies described in the previous work. Again this was attributed to the dominance of the surface stress forces at low frequencies. In this work, a quantitative value for the frequency at which the dominant force transitions from surface stress to electrostatic was calculated and compared to data, with which it agreed well. Next, the relationship between capacitive force and distance was measured in all of the solvents. Here, the authors modeled and measured the effect of each component of the AFM probe (cantilever, cone, and apex) on the overall capacitive force. It was found that, at low frequencies, the force versus distance data matched well with the expression for the force due to the cantilever, suggesting it was the sole contributor to the overall force. At higher frequencies, the cone and apex (tip) became the dominant contributors to the force. These results showed that one must be careful to include all contributions to the force on the cantilever in liquid media. The accumulation of charge can lead to varied affects on the cantilever and its subsequent dynamics.

Each of these exemplary measurements acknowledge that the EDL is always present at the solid-liquid interface. Not only is it present, but its presence needs to be considered carefully. In all of these measurements, the goal was to measure something other than the potential created the EDL at the solid-liquid interface. This potential, however, is the main factor in determining many other important properties of a given interface, such as reaction rates, binding affinity, electrophoretic

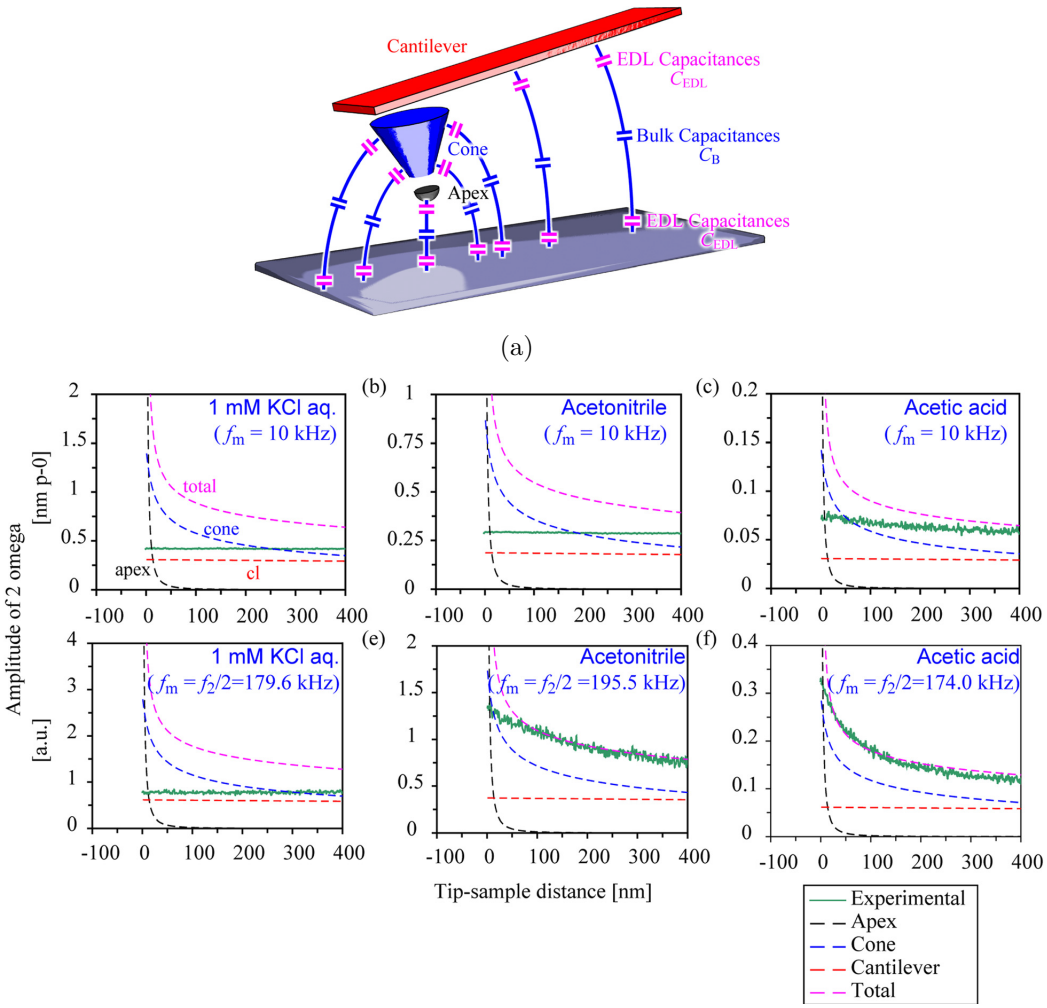

Figure 4.4 (a) The circuit model used by Umeda et al. to describe the dynamics of the cantilever-sample system in various liquid media. (b) 2ω Amplitude vs tip-sample distance data for various liquid media. The data shows that there is a minimum frequency at which the cantilever will be stimulated to oscillate and it varies with solution conditions.*Reprinted from Analysis of capacitive force acting on a cantilever tip at solid-liquid interfaces Umeda, Ken-ichi and Kobayashi, Kei and Oyabu, Noriaki and Hirata, Yoshiki and Matsushige, Kazumi and Yamada, Hirofumi, Journal of Applied Physics, 113, 154311 (2013), with the permission of AIP Publishing.

mobility, and others. For that reason, we will now discuss advancements pertaining to measuring these potentials, with specific focus on measurements done using AFM.

4.3 Measurements of Double Layer Potentials With AFM

Measurements of the electrostatic potentials associated with double layer systems have been in development for nearly 40 years. The first small scale (nanoscopic) measurements of surfaces in electrolytic solutions were carried out using a device devised by Isrealachvili in 1978[**?**]. This device was a modified version of the Surface Force Apparatus (SFA) developed by Tabor, Winterton and Israelachvili several years earlier[**?**]. This version of the device measured the forces between two cylindrical objects immersed in a salt solution as a function of their nanoscopic separations. The separations were measured via the interference fringes of multiple light beams. The forces were measured via the displacement of a calibrated spring system connected to one of the two samples.

Because of the geometrical requirement of the samples, this measurement technique was limited in its uses. Most measurements were done on mica or glass samples or surfactant-modified versions of those two materials. Further iterations of the SFA were introduced and used to measure forces between surfaces in solution. The advent of AFM ushered in a new era in potentials measurements of the solid-liquid interface.

By deriving a useful analytical equation to describe the force between a sphere and plane in solution, Butt was able to quantitatively analyze data from AFM force measurement experiments in different liquid environments[**?**]. He showed that the size of the measured forces were in agreement with those predicted by the derived expression. The data was then used to calculate the screening length, which also agreed well with that predicted by the Debye-Hückel solution of the Poisson-Boltzmann equation.

Later, Ducker and Senden used AFM to measure the forces between similar surfaces to extract quantitative information about surface potentials at a variety of

solution pH's and concentrations[?]. Their results were in agreement with previously measured values using other experimental techniques and calculations. This was one of the earliest reports of using DLVO theory to find fits to experimental data on the force between surfaces in solution. By using similar surfaces, they were able to reduce the number of fit parameters since the two surface potentials were assumed to be equal.

How does the choice of surface effect the analysis of the output data? Recall that the only output of an AFM is the force experienced by the probe. Therefore, if one wishes to extract information about the electrostatic potentials, one needs an expression that relates the force to the various potentials of interest. This has been done in many forms by essentially extending the framework of DLVO theory to new geometries. For instance, the interaction energy as a function of potentials between two spherical particles, each surrounded by diffuse charged layers, was calculated by Hogg and Healy in 1965[?]. Lin et al. used this result to obtain a simple expression for the force between a spherical particle and a planar surface separated by a distance z[?]. This is mentioned specifically because it represents the typical model of the geometry used in AFM experiments. They found that the force for such a geometry is given by

$$F(z) = \frac{4\pi\epsilon\epsilon_0 R\phi_1\phi_2 \exp[-\frac{z}{\lambda}]}{\lambda}, \tag{4.1}$$

where ϕ_1 and ϕ_2 are the potentials of the two surfaces with respect to bulk, R is the sphere radius, ϵ and ϵ_0 are the dielectric constant of the medium and permitivitty of free space, respectively, and λ is the Debye Length. Looking at the form of this expression it becomes clear that both potentials cannot be measured simultaneously. At least not by fitting experimental force data, since the function is indiscriminate of the two potentials. For this reason, one of the surfaces must first be calibrated in that its potential must be known. Only then can the experimental data be fit for the

remaining potential of interest. This calibration step has been handled by a number of researchers in the recent past.

One way to exploit the structure of (4.1) is to create a situation in which the two potentials are equal. This reduces the number of fit parameters by one and induces a single potential parameter such that

$$F(z) = \frac{4\pi\epsilon\epsilon_0 R\phi^2 \exp[-\frac{z}{\lambda}]}{\lambda}. \tag{4.2}$$

For instance, Montes-Ruiz et al. used spherical probes and spherical samples to exploit the symmetric sphere-sphere geometry. The calibration step in their measurements consisted of measuring the force between two spheres of the same material and fitting the data for the single potential. With a calibrated probe particle, they then measured the forces between that probe and various sample particles. Fitting force data to (4.2) algorithmically can only yield the absolute value of the potential parameter. To solve this problem, Hu et al. and many others imported information about the surface chemistry of various materials in order to determine what the sign of the potential must be[**?**, **?**, **?**]. For instance, it is known that alumina surfaces are negatively charged at pH values above 8.1 and positively charged otherwise. Information about various types of materials is plentiful in literature. Details of this imported information will come in a later discussion. Using information of this sort, one can determine the sign of the remaining potential parameter.

Other methods for calibrating the probe have been developed as well. Kumar et al. developed an analytical model and measurement scheme that consisted of a multiple calibration steps plus the measurement step. They employed multi-frequency KFM-type measurements coupled with an analytical expression for the capacitive gradient of the tip-sample system to extract a value for the potential of the AFM probe. They

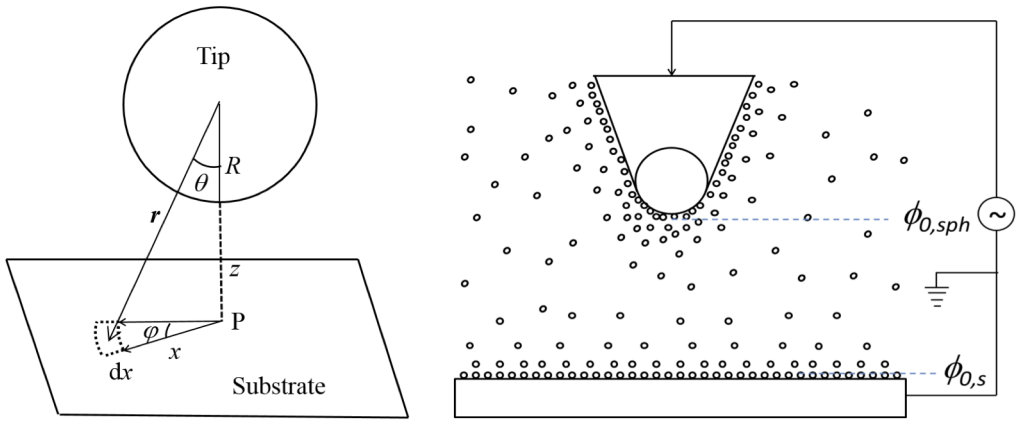

(a) (b)

Figure 4.5 (a) Model of the tip-sample system as proposed by Kumar et al. Only the spherical part of the AFM tip is considered. It is characterized by its radius R. An area element on the planar surface below the sphere is shown. The area element is dA $= (R+z)^2 \tan\theta d\theta d\phi$. (b) Model of tip-sample system in experimental conditions with EDL on each surface. Note the definition of surface potentials $\phi_{0,sph}$ and $\phi_{0,s}$ and their locations with respect to the surfaces.

found that, using their notation,

$$\frac{dC}{dz} = 4\pi\epsilon_0\epsilon_r A\frac{R}{\lambda}\left[2\beta(\Gamma[-1,\beta]+\Gamma[-2,\beta])\exp\left(\frac{R}{\lambda}\right) - (1+\frac{1}{\beta})\exp\left(-\frac{z}{\lambda}\right)\right] + \frac{BV_{AC}^2}{4}, \tag{4.3}$$

where $A = \frac{\phi_{0,t}}{V}$, B is a constant which arises from the contribution of the cone and beam to the overall capacitance, $\beta = \frac{R+\lambda}{z}$, and $\Gamma[\ ]$ is the upper incomplete gamma function. V is the bias potential applied to the AFM tip. Because the measured force in KFM experiments is proportional to the capacitive gradient, this was used to fit the experimental force data for values of A and hence $\phi_{0,t}$. Their measurements are the first to use AFM to measure the potential drop across the Stern layer, which is given by the value of A.

More work has also been done on more accurately modeling the typical AFM probe in the framework of the DLVO theory. Drelich et al. derived a model for a conical tip and flat substrate interaction force that incorporated both the electrostatic contribution as well as forces due to van der Waals interaction[**?**]. To do so, they

modified the model of Parsegian and Gingell, which calculated the force per unit area between two invite plates in a salt solution[**?**]. They did so by adjusting the planar geometry of one of the surfaces to that of a truncated cone with a sphere embedded at the end. They found that for surfaces held at constant potential,

$$\begin{aligned} F(z) = {} & 4\pi\epsilon\epsilon_0\phi_t\phi_s(a_0\exp[-\kappa D] - a_1\exp[-\kappa L_1]) \\ & - 2\pi\epsilon\epsilon_0({\phi_t}^2 + {\phi_s}^2)(a_2\exp[-2\kappa D] - a_3\exp[-2\kappa L_1]) \\ & + \frac{4\pi\epsilon\epsilon_0\kappa}{\tan\alpha}\left[b_1\phi_t\phi_s\exp[-\frac{\kappa}{L_1}] - b_2\frac{\phi_t^2+\phi_s^2}{2}\exp[-2\frac{\kappa}{L_1}]\right], \end{aligned} \tag{4.4}$$

where the first two terms represent the force due to the spherical section of the tip and the last term represents the contribution to the force from the conical section of the tip. Here,

$$\begin{aligned} a_0 &= \kappa R - 1 \\ a_1 &= \kappa R\cos\alpha - 1 \\ a_2 &= a_0 + 0.5 \\ a_3 &= a_1 + 0.5 \\ b_1 &= \left[\mathrm{R}\ \sin\ \alpha - \frac{\mathrm{z}+\mathrm{R}(1-\cos\ \alpha)}{\tan\ \alpha}\right] + \frac{1}{\tan\ \alpha}\left[(L_1 + \frac{1}{\kappa})\right] \\ b_2 &= \left[\mathrm{R}\ \sin\ \alpha - \frac{\mathrm{z}+\mathrm{R}(1-\cos\ \alpha)}{\tan\ \alpha}\right] + \frac{1}{\tan\ \alpha}\left[(L_1 + \frac{1}{2\kappa})\right] \\ L_1 &= \mathrm{z} + \mathrm{R}(1-\cos\ \alpha) \end{aligned} \tag{4.5}$$

Even this model, with its complex structure, suffered from the indiscriminacy of the two potentials. That is, force data cannot be fit to this model with the hope of extracting unique solutions for the two potential parameters.

In this work, the authors first calculated the surface charge density of the sample and converted that to a surface potential via the Grahame equation. Their analysis, similar to other authors, required importing information about the sign of the surface charge of the probe to be used as an input parameter in the fitting of the data.

Experimental investigations of the double layer take many forms. This chapter has focused on AFM-based measurements. Other methods include electrochemical approaches such as impedance spectroscopy and cyclic voltammetry, spectroscopic techniques such as total internal reflection microscopy and X-ray photoelectron spectroscopy (XPS), electrophoretic techniques such as streaming potential measurements, and several others[?, ?, ?, ?, ?, ?]. Every technique or class of techniques has its advantages and drawbacks.

With the basic models of the EDL having been experimentally verified, the focus has shifted to measuring finer and finer contributions to the overall dynamics of the solid-liquid interface. More precise measurements, in concert with computationally derived models, are probing the system at smaller length and time scales.

Chapter 5

Measurements of the Stern and Bulk Potentials of Gold Surfaces

5.1 Theory

This researcher has made progress in the development of a theoretical framework with which one can interpret electrical measurements of the solid-liquid interface made with AFM. In particular, this framework relates the electrostatic potential differences that are measurable with simple AFM experimental techniques in a way that allows for the extraction of two interesting parameters.

The first of those parameters is the potential drop that occurs across the Stern layer with respect to some external reference ground. Typically in AFM experiments, the measured and reported "surface potentials" are actually potential differences, of course. Because of the theoretical underpinnings on which the measurements are interpreted, the potentials are by definition measured with respect to the potential within the bulk of the solution. Furthermore, the potential differences measured are almost exclusively those that occur across only the diffuse layer. Although they are referred to as surface potentials, they actually do not represent the potential of the surface in any direct way. Knowledge of the Stern layer potential is needed in order to relate the potentials drop across the diffuse layer to the potential on the surface with respect to the bulk solution.

While it is widely known that the EDL consists of a compact or Stern layer, which acts as a capacitive element within the overall system, the measurements by Kumar

et al. are the only known instance of AFM being employed to measure the potential drop across the Stern layer[**?**]. Other measurements such as XPS have been used to measure this value, but this required the use of a powerful light source not available in a typical laboratory[**?**].

Complicating the situation even further is the fact that the vast majority of potentials measured in AFM experiments in solution are referenced to the bulk solution potential, which remains unknown in every measurement. In electrochemical experiments, external bias potentials are applied to an electrode and the current across the interface of that electrode is measured. Because the potential of the bulk solution is always unknown, electrochemical measurements rely on standard reference electrodes such as the Standard Hydrogen Electrode (SHE) against which all applied biases are measured. If one's aim is to measurer potentials within the solution, however, this is of little help.

In a typical colloidal probe force measurement, the probe and sample are either insulated by themselves or connected to an external power supply. It is of interest to know how biasing the tip or sample or both will affect the EDL at their respective interfaces with the solution and ,in turn, the forces experienced by the probe. The application of external bias potentials to either surface introduces another electrical reference point (the power supply ground) besides the bulk solution potential and these separate reference points make the measurements much less informative. For instance, if, in a given experiment, one applies one Volt to a metallized AFM tip, what does that really say about its potential with respect to the environment in which the ions in bulk solution find themselves? It is reasonable to suppose that they are already experiencing some potential relative to the tip and thus the meaning of one Volt becomes ambiguous in terms of understanding the effects of the applied potential on the EDL.

Therefore, the second parameter that has been measured in this work is the po-

tential of the bulk solution with respect to an external ground source. With this information, the system can now be characterized in the most complete way shown up to this point.

A measurement scheme complementary to the aforementioned model has also been developed. In this scheme, the AFM tip is calibrated by using a particular tip-sample pair, which induces the type of symmetries mentioned in the previous chapter. To make the subsequent measurements experimentally sound, specific sample designs have also been devised. The theoretical foundations of this work lie within the limits of the Gouy-Chapman and Stern models of the EDL. There is no consideration given to the finite size of ions other than those within the compact layer. The medium is considered to be a uniform dielectric with dielectric constant $\epsilon = 80$. The veracity of this consideration will be discussed later in this chapter. Let us begin by first laying out the framework of the analytic model that has been derived.

Proposed here is a combination of both nomenclature and physical model of an EDL system which rids the system of any ambiguity in terms of potentials and their reference point. Consider an experiment with two electrodes separated by an electrolytic solution. Both electrodes are connected to a common power supply with its own ground. We can map the potentials of all points of interest for two cases; the Gouy-Chapman case in which only a diffuse layer of ions is present and the Stern case in which there is both a diffuse layer and a compact Stern layer. In that case we have the two models in Figure 5.1. Here, the ground of the power supply machine is taken as the zero point and all potentials ($V's$) are referenced with respect to it. All corresponding ϕ's represent differences between those potentials. Looking at the two models separately: in the G-C model, V_s is the potential of the sample with respect to machine ground, V_b is the potential of the bulk solution with respect to machine ground, V_t is the potential of the tip with respect to machine ground. Within the solution, ϕ_{sb} is the potential difference between the sample surface and the bulk solu-

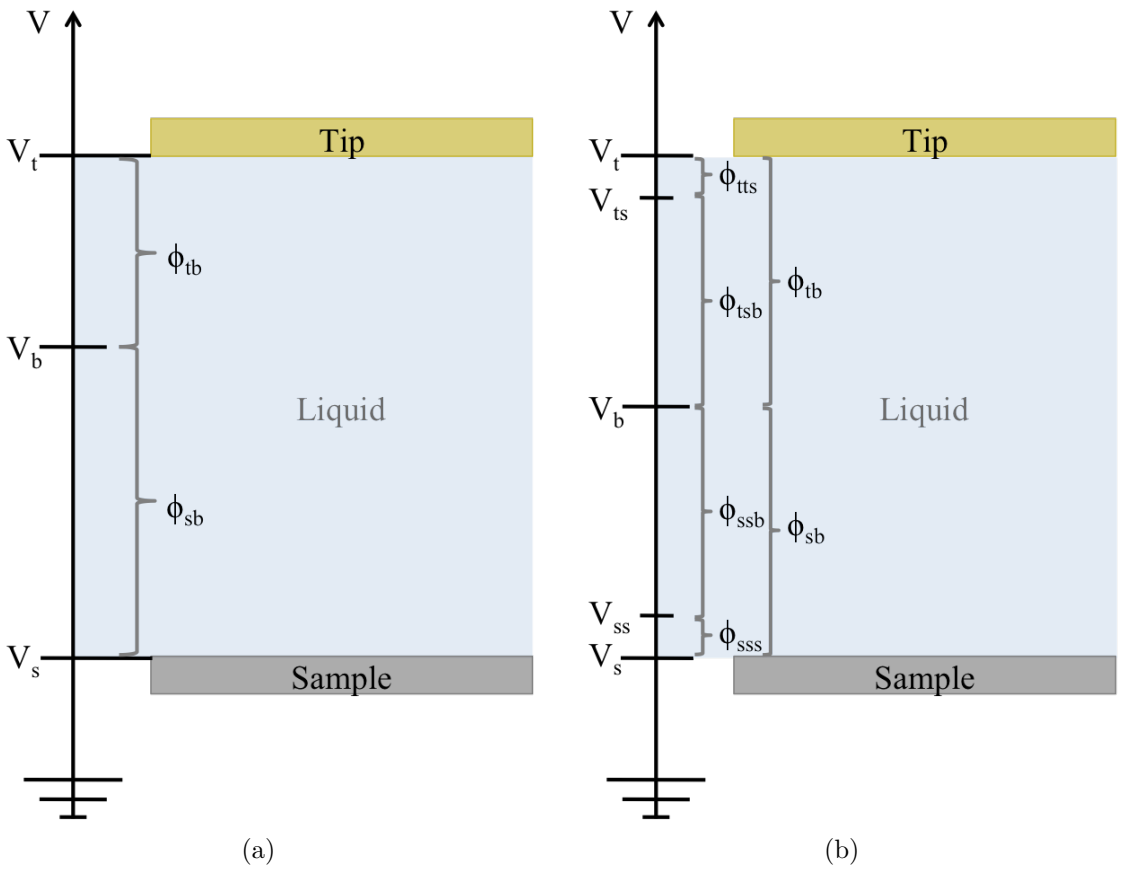

Figure 5.1 Potential level diagrams for the (a) Gouy-Chapman and (b) Stern model. The V's represent potentials measured with respect to the external machine ground and the ϕ's represent potential differences. The ϕ's are what are measured in a typical force experiment. Specifically, ϕ_{ssb} or ϕ_{tsb} is interpreted as the measured potential drop in an AFM force experiment.

tion. This is the diffuse layer potential drop that is almost always referred to as "the surface potential" in literature. The potential drop from the tip surface to the bulk solution has a similar form in this nomenclature, ϕ_{tb}.

In the Stern model of the EDL, the situation is only slightly more complex. V_s, V_t, and V_b retain their same meanings as before. V_{ss} and V_{ts} are the potentials of sample and tip, respectively, at the outer edge of the Stern layer with respect to machine ground. As for the potential drops in the solution,ϕ_{sss} and ϕtts are the potential differences from the electrode surface to the outer edge of the Stern layers, placed at the OHP, of the sample and tip, respectively. Similarly, ϕ_{ssb} and ϕ_{tsb} are

the potential differences between the OHP and the bulk solution. Finally, ϕ_{sb} and ϕ_{tb} are the potential differences between the bulk solution and the surface of the sample and tip, respectively. The reason for this nomenclature becomes more obvious when written mathematically

$$\begin{aligned} \phi_{sb} = V_s - V_b \quad ; \quad \phi_{tb} = V_t - V_b \\ \phi_{sss} = V_s - V_{ss} \quad ; \quad \phi_{tts} = V_t - V_{ts} \\ \phi_{ssb} = V_{ss} - V_b \quad ; \quad \phi_{tsb} = V_{ts} - V_b \end{aligned} \tag{5.1}$$

$$\text{Or more generally} \quad \phi_{ij} = V_i - V_j.$$

Note that the definition of the bulk potential presented here diverges slightly for the one sometimes used in literature. Often, the value of the potential at a point in the bulk solution is given by the work required to bring a charge from infinity to that point. In definition used in this work, however, it is the power supply that determines the potential of the bulk solution that exists between two electrodes. In fact, the bulk potential can be written as

$$V_b = \frac{1}{2}\Delta V + V_q(\Delta V) + V_{b,0}, \tag{5.2}$$

where ΔV is the difference in applied potentials between the two electrodes, V_q is the extra potential generated in the bulk solution by the flow of charge from an electrode across the interface, and $V_{b,0}$ is the potential offset between the machine ground and the interior of the solution. This offset can be measured in an experiment where ΔV is set to zero and it is assumed that $V_q(\Delta V = 0) = 0$. The trans-interface currents and their effect on systems will be discussed in more detail later in this work.

Asserting that the measured force is only due to the diffuse layer, as will be discussed later, the force expression of Lin et al. can be rewritten in this nomenclature as[**?**]

$$F = \frac{4\pi\epsilon\epsilon_0\phi_{tsb}\phi_{ssb}\exp[-\frac{z}{\lambda}]}{\lambda}. \tag{5.3}$$

The introduction of a more descriptive nomenclature has not changed the fact that this equation is degenerate in the two potential values, ϕ_{tsb} and ϕ_{ssb}. That is, there are an infinite number of combinations of values for the two potentials that would yield the same force. Therefore a fit to data of the measured force can not be trusted to produce reliable values of both potentials simultaneously. Still present is the need for some sort of calibration in order to gain knowledge of one the the ϕ's in order to fit force data for the other. Here is where one can implement the symmetric electrode scheme described earlier.

5.2 Tip Calibration

This section outlines the general process for making AFM measurements that can be used as a calibration of the probe in terms of its diffuse layer potential. Typically, gold or platinum AFM probes are used for electrostatic measurements because they are inert in relevant environmental and experimental conditions. That is, they are close to ideal polarizable electrodes, meaning current does not easily flow across the solid-liquid interface and they also have little specific chemistry with most salts. Therefore if we have a gold-coated probe, we can similarly coat a planar sample. From the perspective of an ion in solution, a $\sim 5\mu$m sphere and a planar sample are both infinite planes. The potential profiles of such a situation are given in Figure 5.2. The symmetry that this creates reduces equation (5.3) to

$$F = \frac{4\pi\epsilon\epsilon_0\phi_{tsb}^2 \exp[-\frac{z}{\lambda}]}{\lambda}. \tag{5.4}$$

Looking at (5.4), it is evident that a fit of the force for a value of ϕ_{tsb} will yield only the magnitude of the potential since the fit parameter is actually ϕ_{tsb}^2.

How can we deduce the sign? It is known that different surfaces gather particular charges at given pH conditions. The value of the pH at which no charge gathers on a surface is known as the point of zero charge or isoelectric point (IEP). At pH

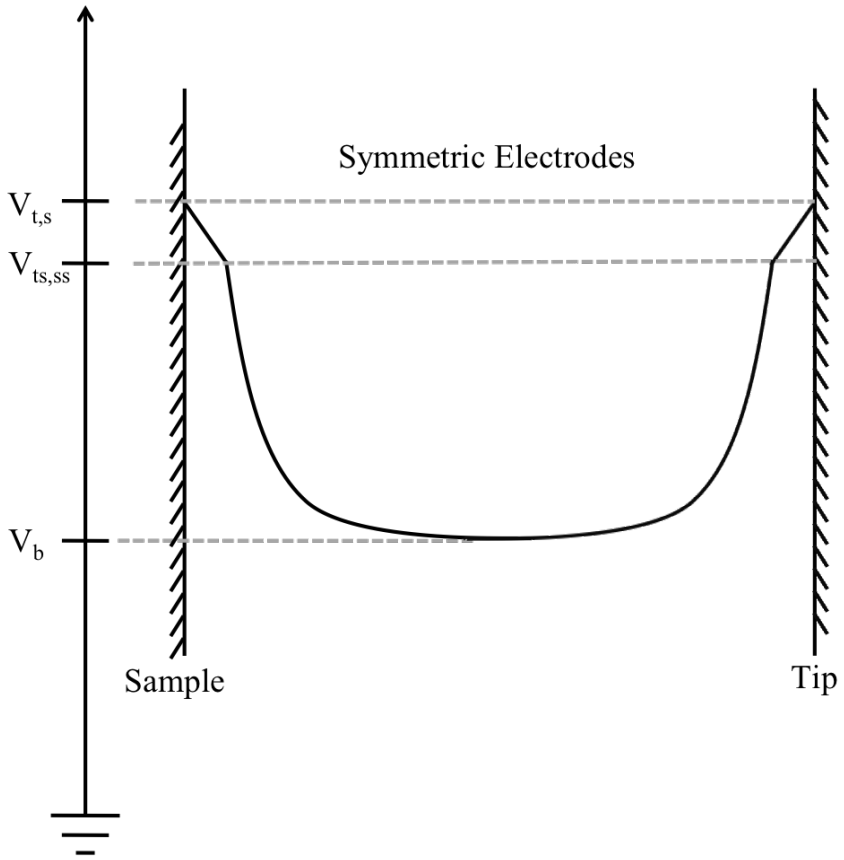

Figure 5.2 The potential profile for the symmetric electrode case. The drops across each region are the same in magnitude on either solid-liquid interface.

values above the IEP, surfaces will obtain net negative charges and positives ones at values below the IEP. This is because the pH is a measure of the ratios of positive hydrogen and negative hydroxide molecules. Higher pH values indicate a higher ratio of hydroxide ions in solution, which will result in more negative charges being driven toward the surface. Given that the IEP of gold is known to be $\sim 3-4$, its surface charge state and hence sign of the diffuse potential drop can be found at any pH[?].

The choice of which surface receives the calibration is arbitrary, but in general, it is more useful to calibrate the probe. With a fully calibrated probe, it is then possible to measure the diffuse layer potential drop of any surface.

5.3 Capacitive Description of the EDL

Of interest to this research is the effect of DC electrode biases on the electrostatic environment at the solid-liquid interface. In particular, we seek to measure the potential at every point in the system. We assert that, with knowledge of the diffuse layer potential differences, one can infer the potential drop across the compact Stern layer, and hence fully characterize the electrostatic environment of the interface.

To make this possible, we use a result obtained first by Grahame in 1947 that shows that the EDL at an interface can be treated as two capacitors in series. Grahame arrived upon this result by relating the charge in the EDL, which has the same magnitude and opposite sign of the charge on the metal surface, to the two potential drops that occur from the surface to the bulk solution in the Gouy-Chapman-Stern model. By doing so he was able to write an expression for the total capacitance of the interface and showed that the resulting equation was identical to that of two capacitors in series[**?**].

It should be noted that the physical solid-liquid interface does not include four separate layers or sheets of charge that one would expect to be present when two capacitors are placed in series into a circuit. In fact, all of the charge on the solution side of the interface resides beyond the OHP in the diffuse layer. The mathematics simply delivers a convenient expression that contains information about both the Stern and diffuse layers of the system. In the more simplistic Gouy-Chapman model there is a single term in the expression for the total capacitance. Figure 5.3 depicts the system with which the EDL can apparently be modeled in the Gouy-Chapman-Stern framework. In this model, the total capacitance of the system, C_T, is given by

$$\frac{1}{C_T} = \frac{1}{C_{st}} + \frac{1}{C_d} \Rightarrow C_T = \frac{C_{st}C_d}{C_{st} + C_d}, \tag{5.5}$$

where C_{st} and C_d are the capacitances per unit area of the Stern and diffuse layers,

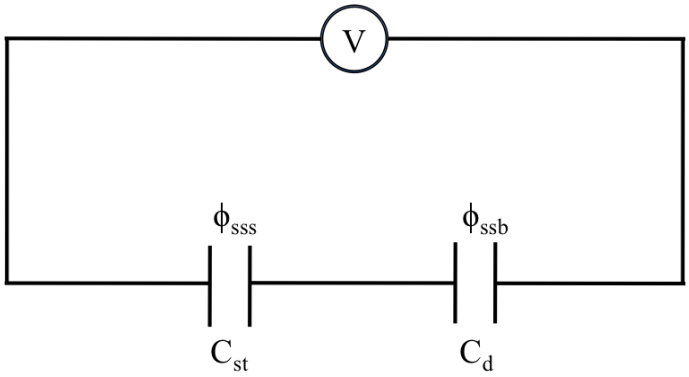

Figure 5.3 Schematic of two capacitors in series model of the EDL system. C_{st} and C_d represent the capacitance of the Stern and diffuse parts of the EDL, respectively. ϕ_{sss} and ϕ_{ssb} are the potential drops across the Stern and diffuse layers, respectively. The physical solid-liquid interface does not contain two separate capacitive elements. All of the charge exists, instead, within the diffuse layer beginning at the OHP.

respectively. The charge density, σ, on the solution side will be governed not by the applied potential, V, directly, but by ϕ_{sb}, which is the total potential drop on the solution side of the interface. Therefore,

$$\sigma = C_T\phi_{sb} = C_{st}\phi_{sss} = C_d\phi_{ssb} \tag{5.6}$$

since capacitors in series have equal charges. Grahame showed that the charge density of the diffuse layer is given by

$$\sigma = \sqrt{8C_0\epsilon\epsilon_0 RT}\sinh\left[\frac{ze\phi_{ssb}}{2kT}\right]. \tag{5.7}$$

Therefore, the capacitance of the diffuse layer can be written as

$$C_d = \frac{\sqrt{8C_0\epsilon\epsilon_0 RT}}{\phi_{ssb}}\sinh\left[\frac{ze\phi_{ssb}}{2kT}\right] \tag{5.8}$$

where C_0 is the ionic concentration of the solution, ϵ is the solution dielectric constant, R is the ideal gas constant, k is Boltzmann's constant, and T is the temperature. It is similarly agreed upon that the capacitance of the Stern layer, which is assumed an ideal linear capacitor, is simply

$$C_{st} = \frac{\epsilon\epsilon_0}{d_{st}}. \tag{5.9}$$

where d_{st} is the thickness of the Stern layer, generally taken to be the radius of a hydrated ion and ϵ is the dielectric constant of the Stern layer, which has been shown to be smaller than the bulk value of 80, but often that value is used as a first approximation[**?**]. With this information known, we can relate all potential drops to the total potential drop across the EDL, ϕ_{sb}, such that

$$\begin{aligned} \sigma &= C_T\phi_{sb} = \sigma_{st} = \sigma_d \\ &= \frac{C_{st}C_d}{C_{st}+C_d}\phi_{sb} = C_{st}\phi_{sss} = C_d\phi_{ssb} \\ \Rightarrow \phi_{sss} &= \frac{C_d}{C_{st}+C_d}\phi_{sb} \\ \text{and} \quad \phi_{ssb} &= \frac{C_{st}}{C_{st}+C_d}\phi_{sb} \end{aligned} \tag{5.10}$$

Dividing these last two and solving for ϕ_{sss}, we get

$$\phi_{sss} = \frac{C_d}{c_{st}}\phi_{ssb} \tag{5.11}$$

Plugging in the capacitance expressions, we get

$$\begin{aligned} \phi_{sss} &= \frac{\frac{\sqrt{8C_0\epsilon\epsilon_0 RT}}{\phi_{ssb}}\sinh[\frac{ze\phi_{ssb}}{2kT}]}{\frac{\epsilon\epsilon_0}{d_{st}}}\phi_{ssb} \\ &= \frac{\sqrt{8C_0\epsilon\epsilon_0 RT}\sinh[\frac{ze\phi_{ssb}}{2kT}]}{\frac{\epsilon\epsilon_0}{d_{st}}}. \end{aligned} \tag{5.12}$$

Therefore, with AFM measurements that yield values of ϕ_{ssb} at different applied V's, it is possible to find a corresponding value of ϕ_{sss}, the potential drop across the Stern layer. Furthermore, since ϕ_{ssb} is measured directly, it can be related to the potential of the bulk solution by $\phi_{ssb} = \frac{C_{st}}{C_d+C_{st}}(V_s - V_b)$. V_s is set during the experiment and hence V_b and V_{ss} can be found for each fitted value of ϕ_{ssb}. In this way, the entire system can be characterized with respect to the same reference point, thus reducing the amount of ambiguity.

Several assumptions have been made in the construction of this analysis, which merit discussion. First is the assumption that there are no Faradaic currents. That is, no charge flows from the electrode to the solution. Is this reasonable? In a

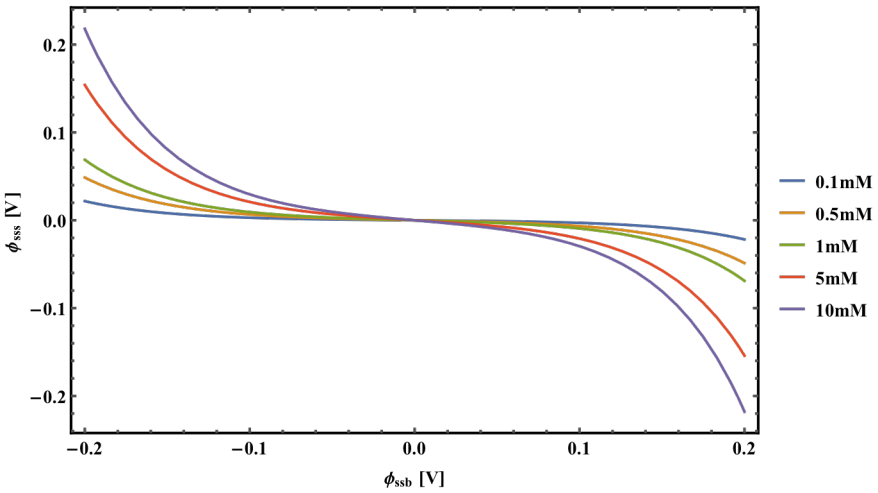

Figure 5.4 Relationship between the potential drops across the two layers as a function of solution concentration. The potential drop across the Stern layer increases as the solution concentration increases.

typical electrochemical experiment, these are the currents that are of interest to the researcher. Our experiments are carefully designed, however, to avoid such currents. The major source of these currents in electrochemical experiments is the reduction and oxidation of electroactive species within the solution itself.

For experiments done using this model, we, by design, have no such electroactive species at the potentials applied to the electrode. More specifically, we typically measure dilute electrolytes such as NaCl of KCl or KNO3, etc. The chemical species within these salts are known to have higher reduction/oxidation potentials than the water in which they are dissolved. For instance, it is known that the reduction potentials of Na^+ and K^+ are -2.71V and -2.92V vs a Standard Hydrogen Electrode (SHE), respectively. For comparison, water molecules are reduced at -0.83V vs SHE. As for anions, the oxidation potentials of Cl^- and NO_3 are -1.36V and 0.8V vs SHE. Water molecules are oxidized at -1.23V vs SHE. Since the Cl^- atoms and water molecules have similar oxidation potentials, both Cl_2 and O_2 gases can be produced at the anode, but only at that applied voltage, which is well above those used in these experiments.

The redox potentials are also affected by the solution pH which may be adjusted during our experiments. However, it will shift all potentials in a similar way. In practice, our experiment will never apply potentials above a few hundred millivolts, so we will catalyze no reactions and produce no Faradaic currents.

The other source of current is the actual flow of charge across the interface. As discussed in section 5.2, we choose electrode/solution combinations that act as ideal polarizable electrodes. In these systems, charge does not flow across the interface, but instead builds on each side of the interface. For these reasons, it can be assumed that no charging of the interface occurs other than that generated by the migration of ions from bulk.

The next assumption holds that the Stern layer does not contribute to the force. Why is this? In the model of the system we have adopted, the region of space between the surface and OHP contains no charge. In this region, a linear potential drop occurs, and it is this potential we wish to probe. The charges of the Stern layer exist at the OHP. An application of Gauss' Law to the probe, assumed to be spherical, shows that the it can be treated as a single point charge located at the sphere's center with a magnitude equal to the net charge on its surface. A Gaussian surface that encompasses only the charges in the Stern layer will encompass the net charge. In the absence of specific adsorption at the surface, this is zero. Hence the force between it and any other charge distribution such as the one on the sample surface, also with a charge-free region out to the OHP, is zero. In this way, we can declare that the Stern layer of charges do not contribute to the measured force. Therefore, all of the force is from the interaction of the two diffuse layers of charge and the force expression can be fit with data to yield values of the diffuse layer potential drop.

Measuring The Stern Potential Drop

The systematic gathering and analysis of data described above has been performed for a small number of solutions at different applied bias potentials. More extensive testing of these systems is likely to yield more interesting results about the limits of the various assumptions made in this model or the underlying Gouy-Chapman-Stern model.

Force curves measured in various solutions with a symmetric probe and sample exhibited the expected repulsive behavior, which was then fit to the force model of Lin et al. The symmetry was induced by coating the probe and sample with identical gold films. It is known that small changes in surface morphology can occur in separate coating processes. Therefore, the probes and samples were coated in a single thermal evaporation process.

Force data was taken at bias potentials of 100mV, 200mV, 300mV, and 400mV. Bias potentials are applied to the tip only, sample only, and to the tip and sample simultaneously in every possible permutation. At least 50 force curves were measured at each applied bias and were then averaged and the average force curve was fit to the force model as shown in Figure 5.5. The diffuse layer potential drops were calculated from the fits. The values of the diffuse layer potential drop are in some agreement with previously reported values for gold surfaces. Barten et al found the diffuse potential drop to change by ∼60mV with an applied bias range of 400mV. Fréchette and Vadnerlick, however, found a larger spread (∼150mV) of measured diffuse layer potential drops over a similar bias range[**?**]. These results are more in line with those found within this work as can be seen in Figure 5.6 From the fitted values of ϕ_{ssb}, corresponding values of ϕ_{sss} were calculated. Results are shown in Figure 5.6.

With knowledge of the potential drops across both parts of the EDL, it is possible

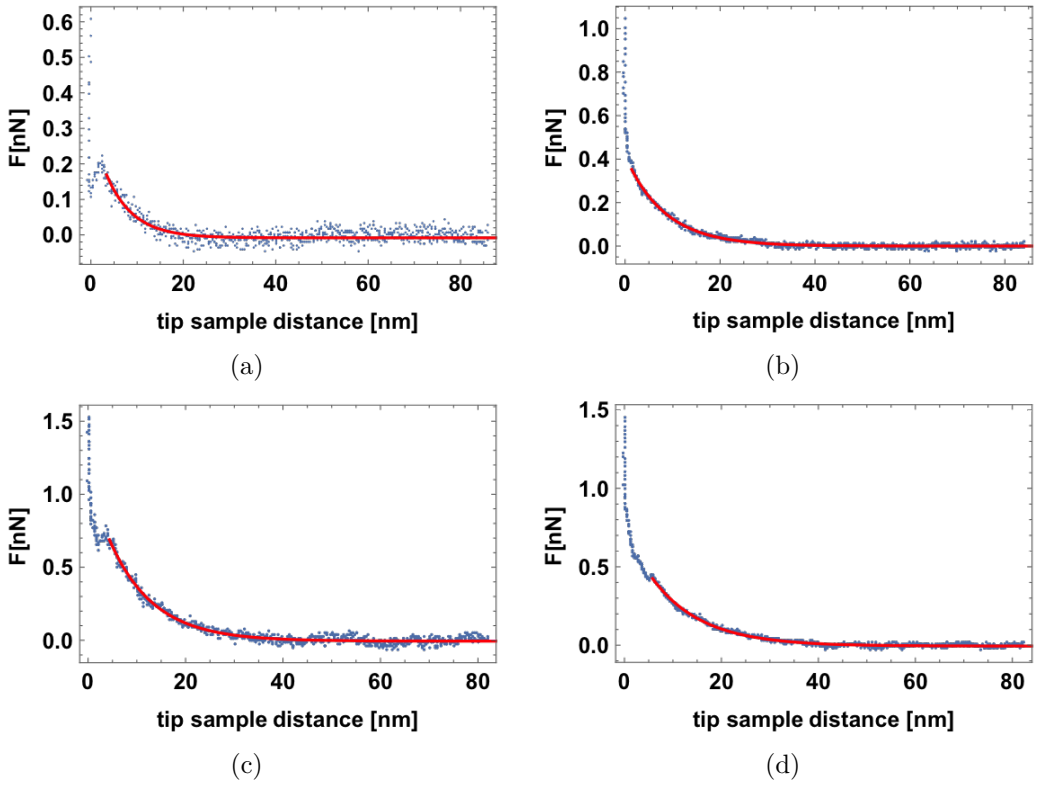

Figure 5.5 Example experimental data from force measurements in 2mM NaCl of the symmetric gold-gold system with sample bias potentials of (a) 100mV, (b)200mV, (c) 300mV, and (d) 400mV. The blue dots represent the data and the red line is the fit of (5.3). A Previous measurement with no applied bias yields the value of ϕ_{tsb}, calibrating the probe. The data in the figure was then fitted for values of ϕ_{ssb}

.

to extract the fractional drop across each layer at different conditions, namely for different applied bias potentials. For instance, the fraction of the total potential drop from surface to bulk that takes place across the Stern layer is given by

$$\alpha_{stern} = \frac{|\phi_{sss}|}{|\phi_{sss}| + |\phi_{ssb}|}. \tag{5.13}$$

The results of this calculation are shown in Figure 5.7.

The final parameter of interest that was calculated using this theoretical framework was the bulk solution potential. While it is unreasonable to expect that the situation behaves in a reasonable way at the high applied bias potentials used for this data, it is still informative to follow through will all the possible calculations. The

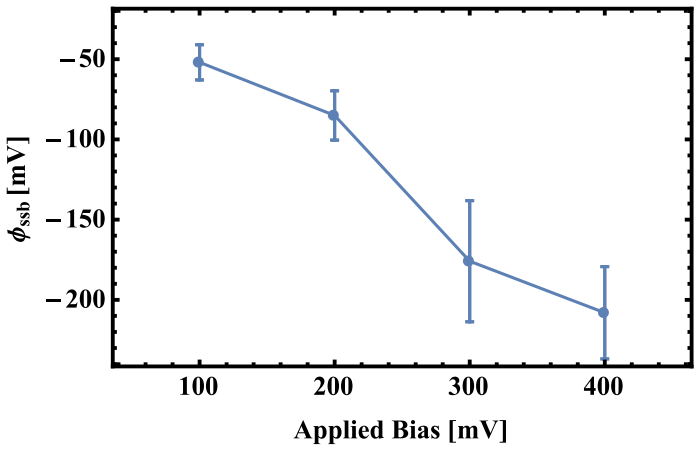

(a)

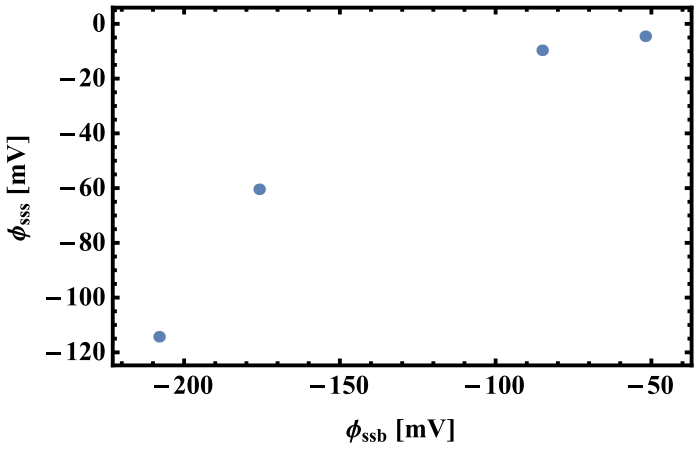

(b)

Figure 5.6 Results from the fitting of experimental data. (a) shows the results for the fit of ϕ_{ssb} directly form force data. The data in (b) is the corresponding set of potential drops across the Stern layer, calculated from (5.12).The red line is a visualization of (5.12)

last line in (5.10) can be inverted to get the value of the bulk potential as a function of the measured diffuse layer potential drop and the applied bias potential. Figure 5.8 shows the results of this process.

As can be seen, the bulk potential values increase sharply with applied bias potentials in the range explored with this data. It is reasonable to assume that at such high biases, the electrode can act in a less than perfectly polarizable way and thus current may flow across the interface, charging the solution. It is also possible that some chemical reactions have been catalyze with these bias potentials, which may

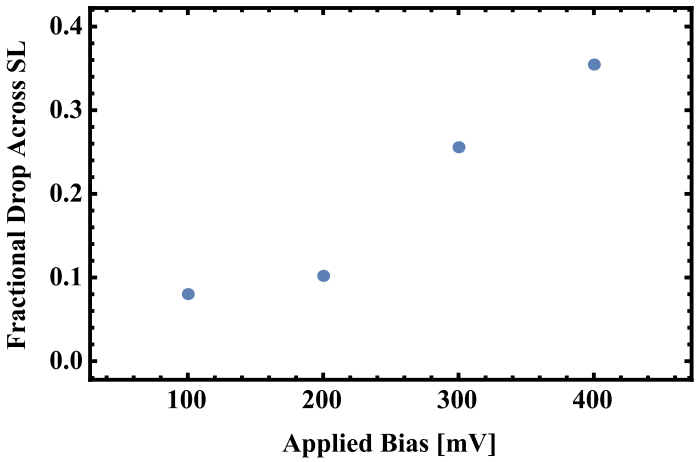

Figure 5.7 The fraction of the total potential drop on the solution side of the solid-liquid interface that occurs over the Stern layer at different applied biases. It appears from the data that the fractional drop is a function of the applied bias.

also affect the value of the bulk potential. Future experiments will be limited to applied biases no higher than 100mV with respect to machine ground.

Another possible reason for the spurious behavior of the calculated values of the bulk potential as a function of applied bias potential comes form the probe calibration step. In the data presented here, the probe was calibrated at no applied bias to either surface. The probe remained unbiased in all experiments and so the value obtained for its potential with respect to the bulk solution, ϕ_{tsb}, was used as an input parameter for the calculation of the sample potentials, ϕ_{ssb} and ϕ_{sss} at various applied bias potentials. However, varying the applied bias to the sample can lead to changes in the bulk potential as defined in this system, and thus ϕ_{tsb} will have a different value at each applied sample bias.

This particular effect is especially prevalent in the data presented here due to the choice of sample. The sample was a gold-coated mica disk approximately 1cm^2 in area. Due to its size, small changes in the sample bias are very likely to affect the bulk liquid potential. With a better sample design, discussed later in this section, this effect can be mitigated. The effects of the large bias potential may be the reason for the larger error in measurements of the diffuse layer potential drop seen in Figure

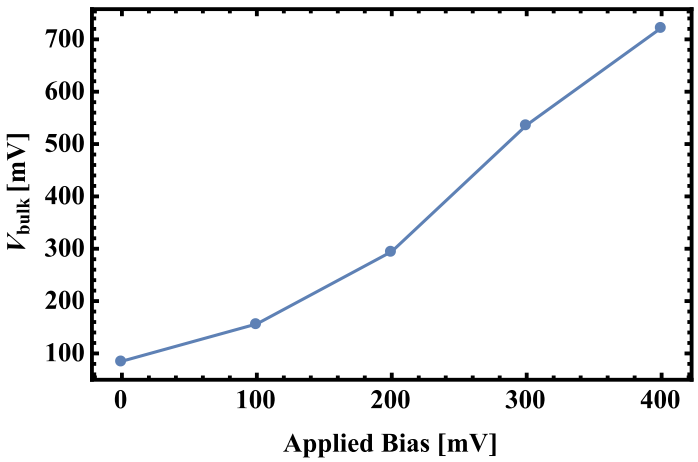

Figure 5.8 Electrostatic potential of the bulk solution with respect to machine ground as a function of the applied bias potential. The bulk potential seems to be strongly affected by the application of bias voltages above 100mV with respect to machine ground, suggesting currents are passing across the interface.

5.6(a).

Finally, in order to perform as many interesting experiments as possible, the design of samples needs to be considered. There are two types of experiments that can utilize the theoretical developments made in this work.

The first type of experiment is one in which there is no variation of the applied bias to the probe or sample. In these measurements, the sample itself and the properties of the EDL of this sample are what is of interest. In this case, the probe needs to be calibrated and then a surface of interest can be measured. Proper sample design can make this process fast, reliable, and robust.

In a typical AFM experiment, the housing that contains the probe may need to be lifted from the sample and replaced if the sample is being replaced for a different one, possibly leading to errors of a few different types. For example, reapproaching the AFM probe to the sample may yield a new angle between the probe and sample surfaces, or the removal of the probe from solution may allow for outside contamination. Therefore, there is a need for a design that has at lest two separate surfaces, one for calibration, and one for testing.

The design proposed here allows for the calibration of the AFM probe and subsequent measurements of other surfaces of interest without removing the AFM probe from the solution to perform the sample exchange. Photolithography makes the generation of patterned samples quite simple. A schematic of the sample design for experiments with no biasing is shown in Figure 5.9(a). The area marked 'C' is the calibration pad and is a surface of the same material as the probe. It is connected to the external power supply via a patterned "wire". The connection to the power supply is done only to set the potential reference point and there are no potentials applied to the probe or sample. The larger, gray region is the sample surface to be probed. It can be a metal, a semiconductor, or a chemically-modified surface, such as one with a self-assembled monolayer (SAM) or polymer deposited. With multiple photolithography steps, it may be possible to create multiple different test regions so that more than one surface can be tested within a single experiment.

In the second type of experiment, the effect of interest is that of a varying applied bias to either the probe or the sample or both. As mentioned previously, this varying applied bias to the surface may have effects on the solution itself that permeate through the entire analysis process. In order to minimize this effect, a simple design that maximizes the constancy of the bulk potential is required.

It is likely that the effect of applied bias on the bulk potential is dominated by the geometry of the two electrodes. Therefore, proposed here for this type of measurement is a simple design that is, in a way, the negative of the sample design for the first type of measurements. In this design, the vast majority of the sample area is the same material as the probe. The sample, whose bias potential may be varied, encompasses a small fraction of the total surface area.

With this design, the probe can be calibrated and its potential with respect to the bulk solution will not change, even when bias potentials are applied to the sample. In this way, the effects of applied biases on the solution side potentials of the sample

can be measured. Figure 5.9(b) shows the design of such a sample. Note the relative sizes of the calibration area and the sample area.

5.5 Conclusions

The research done thus far has led to the development of a model of the electrostatic potential distributions within the EDL. The model is based on agreed upon results and takes a simple approach to relate measured experimental parameters to those that are set by the experimenter. The simple expressions that are derived within the model framework are easily fit to experimental data. Parallel to the development of the model has been the establishment of a measurement scheme that allows for calibration of the AFM probe and subsequent measurements with minimal adjustments to the apparatus. Careful sample design minimizes the experimental error in the collection of data.

With all of these tools, it has been shown that one can measure the potential drop that occurs across the compact Stern layer. It appears in the preliminary work that this value is a function of the applied bias potential. Similarly, one can measure the potential of the bulk solution with respect to machine ground. It also appears to be a function of the applied potential. The measured values of the Stern layer potential drop fit the series capacitors model well, even at large applied biases. Further measurements will focus on smaller applied bias potentials to minimize the detrimental effects discussed earlier.

The values of the bulk potential found in this analysis suggest that the solution underwent charging from the electrode. This violates the assumption that no trans-interface currents are present in the system and is another reason lower potentials will be applied in further tests. This is interesting in itself, for this suggests that this analysis can be used as a way to understand the details of the charging of the solid-liquid interface.

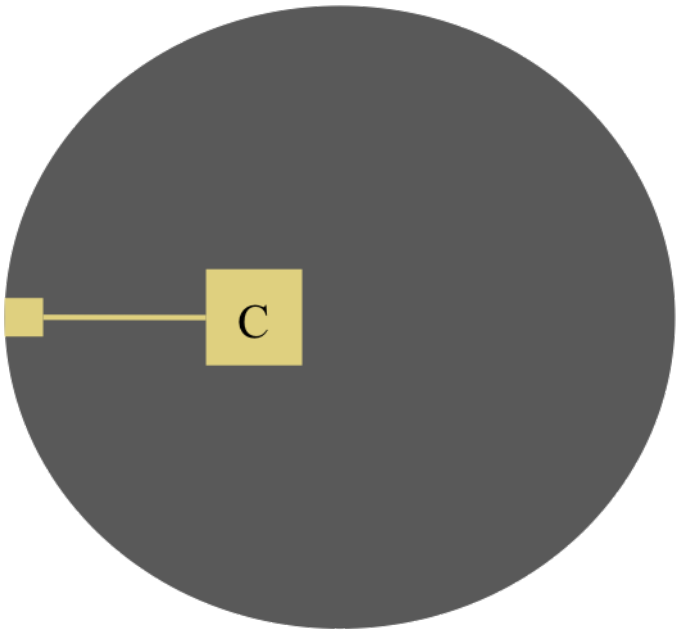

(a)

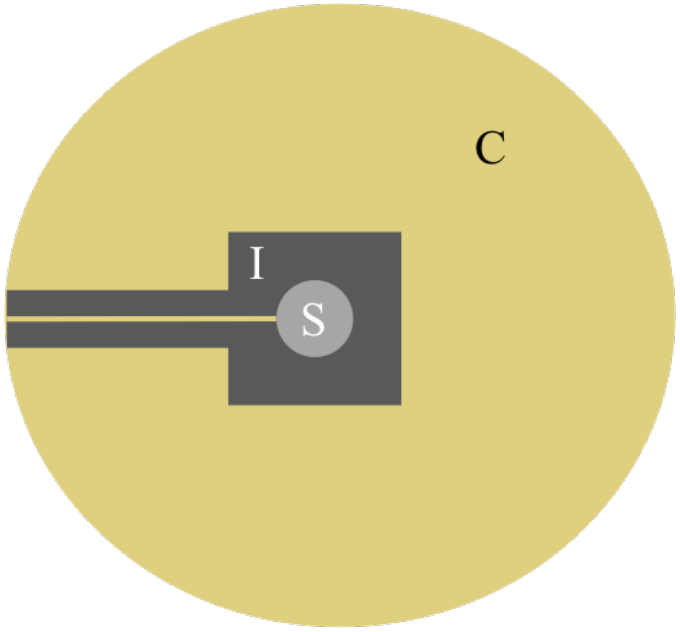

(b)

Figure 5.9 Sample design to be used in the (a) unbiased and (b) biased measurements. The part of the sample marked "C" is the same material as the probe and is used for calibration. The area marked "I" in the second design is an insulating layer and "S" represents the sample surface that will be external biased and subsequently measured.

Bibliography

[1] *Dictionary.com unabridged*, (2015).

[2] Allen J. Bard and Larry R Faulkner, *Electrochemical methods fundamentals and applications*, 2001.

[3] D. Barten, J. M. Kleijn, J. Duval, H. P. v. Leeuwen, J. Lyklema, and M. A. Cohen Stuart, *Double layer of a gold electrode probed by afm force measurements*, Langmuir **19** (2003), no. 4, 1133–1139.

[4] John Bechhoefer, *Feedback for physicists: A tutorial essay on control*, Reviews of Modern Physics **77** (2005), no. 3, 783–836.

[5] J. O. Bockris, M. A. V Devanthan, and K. Mueller, *On the structure of charged interfaces*, Proc. Roy. Soc. **274** (1963), 55–79.

[6] Matthew A. Brown, Zareen Abbas, Armin Kleibert, Richard G. Green, Alok Goel, Sylvio May, and Todd M. Squires, *Determination of surface potential and electrical double-layer structure at the aqueous electrolyte-nanoparticle interface*, Physical Review X **6** (2016), no. 1, 011007–.

[7] Hans-Jürgen Butt, *Measuring electrostatic, van der waals, and hydration forces in electrolyte solutions with an atomic force microscope*, Biophysical Journal **60** (1991), no. 6, 1438–1444.

[8] Hans-Jurgen Butt and Michael Kappl, *Surface and interfacial forces*, 2010.

[9] B. Capella and G. Dietler, *Force-distance curves by atomic force microscopy*, Surface Science Reports **34** (1999), 1–104.

[10] David L. Chapman, *A contribution to the theory of electrocapillarity*, Philosophical Magazine **6** (1913), 475–481.

[11] B. E. Conway, J. O'M. Bockris, and I. A. Ammar, *The dielectric constant of the solution in the diffuse and helmholtz double layers at a charged interface in aqueous solution*, Transactions of the Faraday Society **47** (1951), no. 0, 756–766.

[12] B. Derjaguin and L. Landau, *Theory of stability of strongly charged lyophobic sold and of the adhesion of strongly charged particles in solutions of electrolytes*, Progress in Surface Science **43** (1941), 30–59.

[13] Jaroslaw Drelich, Jun Long, and Anthony Yeung, *Determining surface potential of the bitumen-water interface at nanoscale resolution using atomic force microscopy*, The Canadian Journal of Chemical Engineering **85** (2007), no. 5, 625–634.

[14] William A. Ducker, Tim J. Senden, and Richard M. Pashley, *Measurement of forces in liquids using a force microscope*, Langmuir **8** (1992), no. 7, 1831–1836.

[15] Jonathan Ennis, Stjepan Marčelja, and Roland Kjellander, *Double layer modelingeffective surface charge for symmetric electrolytes in the primitive model double layer*, Electrochimica Acta **41** (1996), no. 14, 2115–2124.

[16] Joëlle Fréchette and T. Kyle Vanderlick, *Double layer forces over large potential ranges as measured in an electrochemical surface forces apparatus*, Langmuir **17** (2001), no. 24, 7620–7627.

[17] Nir Gavish and Keith Promislow, *Dependence of the dielectric constant of electrolyte solutions on ionic concentration*, arXiv (2012).

[18] Brian Giera, Neil Henson, Edward M. Kober, M. Scott Shell, and Todd M. Squires, *Electric double-layer structure in primitive model electrolytes: Comparing molecular dynamics with local-density approximations*, Langmuir **31** (2015), no. 11, 3553–3562.

[19] Marcel Giesbers, J. Mieke Kleijn, and Martien A. Cohen Stuart, *The electrical double layer on gold probed by electrokinetic and surface force measurements*, Journal of Colloid and Interface Science **248** (2002), no. 1, 88–95.

[20] Louis George Gouy, *On the constitution of the electric charge on the surface of an electrolyte*, J. Phys. Thoer. Appl **9** (1910), no. 1, 457–468.

[21] David C. Grahame, *The electrical double layer and the theory of capillarity*, Chemical Reviews **41** (1947), 441–501.

[22] G. Gramse, A. Dols-Perez, M.A Edwards, L. Fumagalli, and G. Gomila, *Nanoscale measurement of the dielectric constant of supported lipid bilayers in aqueous solutions with electrostatic force microscopy*, Biophysical Journal **104** (2013), 1257–1261.

[23] G. Gramse, M.A Edwards, L. Fumagalli, and G. Gomila, *Dynamic electrostatic force microscopy in liquid media*, Appl. Phys. Lett. **101** (2012).

[24] J.B Hasted, D.M. Rittson, and C.H. Collie, *Dielectric properties of aqueous ionic solutions. parts i and ii*, J. Chem. Phys. **16** (1948).

[25] R. Hogg, T.W. Healy, and D.W Fuerstenau, *Mutual coagulation of colloidal dispersions*, trans. Faraday Soc. **66** (1965), 1638–1651.

[26] Kai Hu, Fu-Ren F. Fan, Allen J. Bard, and Andrew C. Hillier, *Direct measurement of diffuse double-layer forces at the semiconductor/electrolyte interface using an atomic force microscope*, The Journal of Physical Chemistry B **101** (1997), no. 41, 8298–8303.

[27] Jacob Israelachvili, *Salvation forces and liquid structure, as probed by direct force measurements*, Acc. Chem. Res **20** (1987), 415–421.

[28] Jacob N. Israelachvili and Gayle E. Adams, *Measurement of forces between two mica surfaces in aqueous electrolyte solutions in the range 0-100 nm*, J. Chem. Soc., Faraday Trans. 1 **74** (1978), 975–1001.

[29] Bharat Kumar and Scott Crittenden, *Stern potential and debye length measurements in dilute ionic solutions with electrostatic force microscopy*, Nanotechnology **24** (2013).

[30] Stanislaw Lamperski, Monika Pluciennik, and Christopher W. Outhwaite, *The planar electric double layer capacitance for the solvent primitive model electrolyte*, Physical Chemistry Chemical Physics **17** (2015), no. 2, 928–932.

[31] Yuncheng Liang, N. Hilal, P. Langston, and V. Starov, *Interaction forces between colloidal particles in liquid: Theory and experiment*, Adv. Colloid and Interface Science **134-135** (2007), 151–166.

[32] Xue Yun Lin, Francois Creuzet, and Herve Arribart, *Atomic force microscopy for local characterization of surface acid-base properties*, The Journal of Physical Chemistry **97** (1993), no. 28, 7272–7276.

[33] F. Javier Montes Ruiz-Cabello, Gregor Trefalt, Plinio Maroni, and Michal Borkovec, *Electric double-layer potentials and surface regulation properties measured by colloidal-probe atomic force microscopy*, Physical Review E **90** (2014), no. 1, 012301–.

[34] Chiara Neto, Drew R Evans, Elmar Bonaccurso, Hans-Jürgen Butt, and Vincent S J Craig, *Boundary slip in newtonian liquids: a review of experimental studies*, Reports on Progress in Physics **68** (2005), no. 12, 2859.

[35] Hrishikesh V. Panchawagh, T.L. Sounart, and R. Mahajan, *A model for electrostatic actuation in conducting liquids*, J. Microelectromechanical Systems **18** (2009), 1105–1117.

[36] V Adrian Parsegian and David Gingell, *On the electrostatic interaction across a salt solution between two bodies bearing unequal charges*, Biophysical Journal **12** (1972), no. 9, 1192–1204.

[37] M. Sastre and J.A Santaballa, *A note on the meaning of the electroneutrality condition for solutions*, Textbook Forum.

[38] Peter J. Scales, Franz Grieser, Thomas W. Healy, Lee R. White, and Derek Y. C. Chan, *Electrokinetics of the silica-solution interface: a flat plate streaming potential study*, Langmuir **8** (1992), no. 3, 965–974.

[39] D. Tabor and R. H. S. Winterton, *Surface forces: Direct measurement of normal and retarded van der waals forces*, Nature **219** (1968), no. 5159, 1120–1121.

[40] Ken-Ichi Umeda, Noriyaki Oyabu, Kei Kobayashi, YPshiki Hirata, Kazumi Matsushige, and Hirofumi Yamada, *High-resolution frequency-modulated atomic force microscopy in liquids using electrostatic excitation method*, Appl. Phys. Expr. **3** (2010).

[41] ———, *Analysis of capacitive force acting on a cantilever tip at solid/liquid interface*, J. Appl. Phys. **113** (2013).

[42] E.J.W Verwey and J. TH. G Overbeek, *Theory of the stability of lyophobic colloids*, 1948.

[43] Herman von Helmholtz, *Some laws concerning the distribution of electric currents in volume conductors with applications to experiments on animal electricity*, Annalen der Physik und Chemie **165** (1853), no. 6, 211–233.

[44] Peiming Wang and Andrzej Anderko, *Computation of dielectric constants of solvent mixtures and electrolyte solutions*, Liquid Phase Equilibria **186** (2001), 103–122.